Human Molecular Genetics, 2024, Vol. 33, 1, 12–32
https://doi.org/10.1093/hmg/ddad154
Advance access publication date 15 September 2023
Original Article

Systemic proteome phenotypes reveal defective metabolic flexibility in Mecp2 mutants

Stephanie A. Zlatic[1,*], Erica Werner[1,†], Veda Surapaneni[1,†], Chelsea E. Lee[1,†], Avanti Gokhale[1], Kaela Singleton[1], Duc Duong[2], Amanda Crocker[3], Karen Gentile[4], Frank Middleton[4], Joseph Martin Dalloul[5], William Li-Yun Liu[5], Anupam Patgiri[5], Daniel Tarquinio[6], Randall Carpenter[7], Victor Faundez[1,*]

[1]Department of Cell Biology, Emory University, 615 Michael Steet, Atlanta, GA 30322, United States
[2]Department of Biochemistry, Emory University, 1510 Clifton Rd NE, Atlanta, GA 30322, United States
[3]Program in Neuroscience, Middlebury College, Bicentennial Way, Middlebury, VT 05753, United States
[4]Department of Neuroscience and Physiology, SUNY Upstate Medical University, 505 Irving Avenue, Syracuse, NY 13210, United States
[5]Pharmacology and Chemical Biology, Emory University, 1510 Clifton Rd NE, Atlanta, GA 30322, United States
[6]Center for Rare Neurological Diseases, 5600 Oakbrook Pkwy, Norcross, GA 30093, United States
[7]Rett Syndrome Research Trust, 67 Under Cliff Rd, Trumbull, CT 06611, United States

[*]Corresponding authors. Victor Faundez, Department of Cell Biology, Emory University, Atlanta, GA 30322, United States. E-mail: vfaunde@emory.edu; Stephanie A. Zlatic, Department of Cell Biology, Emory University, Atlanta, GA 30322, United States. E-mail: szlatic@gmail.com
[†]Erica Werner, Veda Surapaneni and Chelsea E. Lee contributed equally.

Abstract

Genes mutated in monogenic neurodevelopmental disorders are broadly expressed. This observation supports the concept that monogenic neurodevelopmental disorders are systemic diseases that profoundly impact neurodevelopment. We tested the systemic disease model focusing on Rett syndrome, which is caused by mutations in *MECP2*. Transcriptomes and proteomes of organs and brain regions from *Mecp2*-null mice as well as diverse *MECP2*-null male and female human cells were assessed. Widespread changes in the steady-state transcriptome and proteome were identified in brain regions and organs of presymptomatic *Mecp2*-null male mice as well as mutant human cell lines. The extent of these transcriptome and proteome modifications was similar in cortex, liver, kidney, and skeletal muscle and more pronounced than in the hippocampus and striatum. In particular, *Mecp2*- and *MECP2*-sensitive proteomes were enriched in synaptic and metabolic annotated gene products, the latter encompassing lipid metabolism and mitochondrial pathways. *MECP2* mutations altered pyruvate-dependent mitochondrial respiration while maintaining the capacity to use glutamine as a mitochondrial carbon source. We conclude that mutations in *Mecp2*/*MECP2* perturb lipid and mitochondrial metabolism systemically limiting cellular flexibility to utilize mitochondrial fuels.

Graphical Abstract

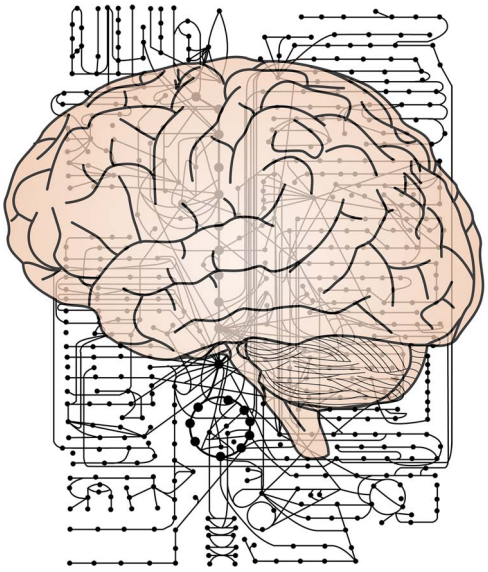

Mouse tissues and cells mutated in the Rett syndrome gene Mecp2 reveal defects in the utilization of fuels by the mitochondria.

Keywords: MECP2; mitochondria; pyruvate; autism; neurodevelopmental disorder

Received: June 29, 2023. **Revised:** September 1, 2023. **Accepted:** September 11, 2023.

Introduction

Rett syndrome is a neurodevelopmental disorder caused by loss-of-function mutations in the epigenetic transcriptional regulator *MECP2* [1–3]. To date, the study of human and animal models of Rett and other neurodevelopmental disorders has primarily focused on the brain. The devastating nature of the neurological and behavioral phenotypes that characterize this and other monogenic neurodevelopmental disorders has rightly justified this focus on neuronal mechanisms of disease [3]. However, the protein products of the *MECP2* and other neurodevelopmental disease genes are widely expressed, and non-neuronal disease phenotypes [4], support the proposition that Rett and other neurodevelopmental disorders may be systemic diseases that profoundly impact neurodevelopment [5–7]. Such conceptualization could enhance biomarker and therapeutic discovery expanding the focus to organs, systems, and fluids beyond the brain and cerebrospinal fluid. Other tissues and cells from patients and animal models could act as a proxy for brain disease, thus empowering discovery of disease mechanism and therapies.

The systemic metabolic disease model of Rett syndrome was formulated before the identification of *MECP2* as the causative gene defect [5]. This idea originated from the Rett syndrome resemblance to mitochondrial diseases and patient alterations pyruvate and lactate levels in biofluids [8–10]. In fact, subjects with MECP2 mutations can manifest disease as a mitochondrial disorder [11]. Numerous studies in humans and in animal models of this disease document the systemic nature of Rett syndrome [5–7]. Humans affected by Rett syndrome have symptoms associated with the respiratory, cardiovascular, digestive, endocrine and musculoskeletal systems [5–7]. *Mecp2* mutant mouse models identify phenotypes in adipose tissue, respiratory, and digestive organs that are cell-autonomous and cannot be attributed simply to defects in organ innervation. Cell-type specific ablation of the *Mecp2* gene in adipocytes, lung epithelial cells, and hepatocytes alters cellular metabolism at the expense of cholesterol, fatty acid, and mitochondrial pathways [12–14]. These *Mecp2* mutant phenotypes can be corrected with genetic or pharmacologic therapeutics that target specific pathways [15, 16]. This growing evidence supports the hypothesis that Rett syndrome is a systemic metabolic disease [5–7].

We unbiasedly evaluated the systemic effects of *Mecp2* mutations by defining the transcriptome and proteome of organs and brain regions from *Mecp2*-null mice. Profound alterations of transcriptomes and proteomes were identified in the brain and organs of *Mecp2*$^{tm1.1Bird/y}$ animals before the appearance of overt phenotypes. Alterations in the transcriptome and proteome are most pronounced in the brain cortex, liver, kidney and skeletal muscle. *Mecp2*-sensitive proteomes are enriched in metabolic annotated gene products for lipid metabolism and mitochondrial pathways across diverse tissues. Importantly, the proteome of the cortex, the most affected brain region, was comparably enriched for both synaptic and mitochondrial annotated proteins. These analyses indicated that a mitochondrial and lipid metabolic hub is perturbed in *Mecp2* tissues and impairs pyruvate-dependent mitochondrial function. We conclude that mutations in *Mecp2/MECP2* systemically alters lipid and mitochondrial metabolism. We propose that compromised metabolic flexibility, flexibility in the utilization of carbon sources by mitochondria, is a systemic mechanism of neurodevelopmental disease.

Material and methods

Animals

All animal procedures and husbandry were approved by Emory University's Institutional Animal Care and Use Committee. The Mecp2-null mouse model, B6.129P2(C)-Mecp2$^{tm1.1Bird}$/J (Cat: 003890 RRID: IMSR_JAX:003890), was purchased from The Jackson Laboratory at 5–6 weeks of age and housed within Emory University's Division of Animal Resources for about 4 days before tissue collection.

Mouse tissue dissection

Mice were euthanized by CO_2 asphyxiation and tissues dissected at 6 weeks of age. Tissue collection was done in the morning and animals were sacrificed by alternating wild type and mutant genotypes to minimize circadian rhythm impact. Liver, kidney, whole brain, and skeletal muscle from the hind quarters (gluteus maximus, rectus femoris or vastus lateralis) of the mouse was removed and washed in ice cold phosphate buffered saline. For micro-punch dissections, all tools and surfaces for dissection were prechilled. Whole brain was transferred to an aluminum coronal slicing matrix with 1.0 mm slice intervals (Zivic Cat: BSMAS001-1 and BSMYS001-1) and sliced with single edge razors. Slices were laid out on an aluminum block and a micro-punch tool kit (Stoelting Cat: 57401) with 1.00 mm punch (Stoelting Cat: 57397) was used to micro-dissect from hippocampal, audio-visual region of cortex, and striatal region. Punches from the left and right hemispheres were pooled for approximately six punches per region. The remaining cortex from all the coronal slices was collected for bulk cortical samples. All samples were flash frozen with liquid nitrogen and stored at −80°C [17].

Mouse primary culture

All tools were sterilized and dissection reagents prechilled. Postnatal day 0–2 pups were euthanized by decapitation. Whole brain was removed and washed in HBSS/10 mM HEPES. Cortex was dissected from the whole brain, cut into 5–6 smaller pieces and digested in prewarmed trypsin solution for 10 min. Cortical pieces were then washed briefly in HBSS/10 mM HEPES twice and transferred to MEM solution consisting of MEM (Sigma M4655) with 10 mM HEPES (Gibco 15630-080), 33 mM D-glucose (Sigma G8769), and 10% FBS (VWR 97068-085) solution. Tissue was triturated 8 times through a fire polished glass pipette. Suspended cells were collected and gently centrifuged for 5 min at 130 RCF, 4°C. Supernatant was removed and cells were resuspended in fresh MEM/HEPES/D-glucose/FBS solution. Cells were plated onto 0.01% poly-L-lysine (Sigma P4707) and 2 $\mu g/cm^2$ laminin (Sigma L2020) coated dishes and cultured in a humidified 37°C, 5% CO^2 incubator. After cells had settled, approximately 2 h, media was changed to Neurobasal (Gibco 21103-049) supplemented with 1× B27 (Gibco 17504-044) and 2 mM L-glutamine. Half the volume of media was changed out every 2–3 days thereafter until assayed at 14 days *in vitro*.

Tissue culture

Control and two clonal MECP2 knock out (2_7 and H4) LUHMES cell lines were gifts from Dr Adrian Bird [18]. Cells were passaged in Advanced DMEM/F12 (Gibco 12634-010) supplemented with 1× N2 (Gibco 17502048), 2 mM L-glutamine (Sigma

G7513), and 40 μg/ml FGF (R&D Systems, 4114-TC) at 2 000 000–500 000 cells/75 cm^2 flask. Three million cells/75 cm^2 were pre-differentiated for 48 h in differentiation media, lifted, and seeded at approximately 1 million cells/cm^2 onto assay plates coated with poly-L-ornithine 44 μg/ml (Sigma P3655) and fibronectin 1 μg/ml (Sigma F1141) in differentiation media. Differentiation media consists of Advanced DMEM/F12 (Gibco 12634-010) supplemented with 1× N2 (Gibco 17502048), 2 mM L-glutamine (Sigma G7513), 1 mM DbcAMP (Sigma D0627) 1 μg/ml tetracycline (Sigma T7660) and 2 ng/ml GDNF (R & D Systems 212-GD). MECP2 KO SHSY5Y cells were developed with Synthego. Synthego used guide RNA sequence CCACTCTGCTGAGCCCGCAG, for genome editing of MECP2 at exon 3, in Cas9-gRNA ribonucleoprotein complexes. A knock-out pool of 93% efficiency was diluted to clonal populations. Clones were confirmed by Sanger sequencing and Western blot. Cells were cultured in DMEM (Corning 10-013-CV) with 10% FBS (VWR 97068-085) at 37°C, 5% CO^2. For differentiation, approximately 40 000 cells/cm^2 were seeded onto plates coated with 0.01% poly-L-lysine (Sigma P4707) per manufacturer's protocol and switched to differentiation media consisting of Neurobasal (Gibco 21103-049) supplemented with 1× B27 (Gibco 17504-044), 500 μM L-glutamine (Sigma G7513), and 1 mM DbcAMP (Sigma D0260) for 3 days and then assayed. MECP2 knock out HAP1 cells from Horizon Discovery (Cat: HZGHC001102c010, RRID: CVCL_SX72) were cultured in IMDM (Lonza, 12-722F) supplemented with 10% FBS (VWR 97068-085) in a humidified, 37°C, 10% CO^2 incubator. For MECP2-GFP rescue of HAP1 cells, pEGFP-N1_MeCP2(WT) was a gift from Adrian Bird (Addgene plasmid #110186; RRID:Addgene_110186), GFP only vector was created by digesting pEGFP-N1_MeCP2(WT) with BamHI and BglII to remove the MECP2 insert and ligated with T4 DNA ligase. Plasmids were transfected to HAP1 cells using FUGene according to manufactures protocol in Optimem Media (Gibco 31985070). Transfected cells were selected with G418 selection 600 μg/ml in growth media 48 h after transfection media was added. Transfected cells were diluted to clonal populations and expanded for assay. For Galactose switch assays, 24 h before assay, HAP1 cells were incubated in a basal DMEM (Gibco A14430-01) supplemented with 10% dialyzed FBS (Hyclone SH30079.03), 1 mM sodium pyruvate, 2 mM L-glutamine, 96 nM sodium selenite, non-essential amino acids, and either 10 mM glucose or 10 mM galactose. In the case of L-glutamine exclusion, the L-glutamine was not added to either the glucose or galactose version of the media. See supplementary table 1 for cell details.

Seahorse oximetry

Seahorse XFe96 FluxPaks (Agilent 102416-100) were hydrated at 37°C for approximately 24 h in Seahorse XF Calibrant solution (Agilent 100840-000). Cells were plated on Agilent Seahorse XF96 V3-PS Microplates (Agilent 101085-004) approximately 24 h before stress tests. Seahorse stress test media consisted of Seahorse XF base medium (Agilent 103334-100) or Seahorse XF DMEM base medium pH 7.4 (Agilent 103575-100) supplemented with 1 mM sodium pyruvate (Sigma S8636), 2 mM L-glutamine (Sigma G7513), and 10 mM D-glucose (Sigma G8769), or 10 mM galactose. For AZD7545 (Selleckchem) experiments, AZD7545 was added to seahorse assay media at 10 μM, 5 μM, 2 μM, 1 μM, 0.5 μM, 0.1 μM, and 0.05 μM AZD7545. Figures and the table below describe the exact components for each experiment. On the day of analysis, cells were washed twice in 37°C warmed Seahorse analysis medium and then the volume was brought to180 μl one hour prior to assay and incubated at 37°C in the absence of CO^2 injection. For AZD7545 treatment, warmed media was added 2 h prior to assay start time. In the case of nutrient starvation, warmed media was added and the assay was immediately started. The mitochondrial stress test was run as per Agilent Seahorse protocols with Seahorse Wave Software (Agilent). Seahorse Wave Software data collection was as per manufactures conditions. For standard mitochondrial stress tests, oxygen consumption rates and extracellular acidification rates were collected 3 times for each phase of the stress test with a 3-min mix step followed by 3 min of measurement. FluxPak ports were loaded with stress test drugs at a 10× concentration of the final well concentration. Stress tests consisted of Oligomycin A (Sigma 75351), Carbonyl cyanide 4-(trifluoromethoxy) phenylhydrazone, FCCP (Sigma C2920), and Rotenone (Sigma R8875) and Antimycin A (Sigma A8674) at injections a, b, and c respectively. For nutrient starvation stress tests, the basal measurements were collected 40 times (about 2.5 h) with 3-min mix steps followed by 3 measurements with 3-min mix steps after each injection. Well concentrations of stress test drugs were cell type dependent and described below. All seahorse microplates were normalized by total protein using the Pierce BCA Protein Assay Kit (Thermo 23227) as per protocol with a BSA protein standard. The BCA assay absorbance was read by a Biotek microplate reader using Gen5 software. Seahorse oximetry data analysis was done with Agilent Wave Software Report Generator and Microsoft Excel. Mouse primary culture: 20 000 cells/well, 2.0 μM oligomycin, 0.5 μM FCCP, 1.0 μM rotenone, 1.0 μM antimycin A, 17.5 mM D-glucose. LUHMES: 40 000 cells/well, 2.0 μM oligomycin, 0.25 μM FCCP, 1.0 μM rotenone, 1.0 μM antimycin. HAP1: 400 000 cells/well, 2.0 μM oligomycin, 0.125 μM FCCP, 1.0 μM rotenone, 1.0 μM antimycin A. SHSY5Y: 30 000 cells/well, 2.0 μM oligomycin, 0.25 μM FCCP, 1.0 μM rotenone, 1.0 μM antimycin A. Media conditions are in Table 1.

Table 1. Seahorse stress test assay media components.

Fig. 5A–L, N–P	Seahorse XF DMEM base medium, 1 mM sodium pyruvate, 2 mM L-glutamine, 10 mM D-glucose
Fig. 6B–D	Seahorse XF base medium, 1 mM sodium pyruvate
Fig. 6E–G	Seahorse XF base medium
	Seahorse XF base medium, 1 mM sodium pyruvate
	Seahorse XF base medium, 1 mM sodium pyruvate, 2 mM L-glutamine, 10 mM D-glucose
Fig. 6H	Seahorse XF DMEM base medium, and 0 mM, 0.125 mM, 0.25 mM, 0.5 mM, 1.0 mM, or 2.0 mM sodium pyruvate
Fig. 6I	Seahorse XF DMEM base medium, and 0 mM, 0.5 mM, or 2 mM L-glutamine
Fig. 7B–E	Seahorse XF DMEM base medium, 1 mM sodium pyruvate, 2 mM L-glutamine, 10 mM D-glucose
	Seahorse XF DMEM base medium, 1 mM sodium pyruvate, 2 mM L-glutamine, 10 mM galactose
	Seahorse XF DMEM base medium, 1 mM sodium pyruvate, 10 mM D-glucose
	Seahorse XF DMEM base medium, 1 mM sodium pyruvate, 10 mM D-galactose
Fig. 7I–K	Seahorse XF base medium, 1 mM sodium pyruvate

Resipher oximetry

HAP1 Control and MECP2 Knock-out cells were seeded at 2000 cells per well in a NUNC 96-well microplate (Thermo Scientific, Cat# 269787) with 200 μl standard growth media (above) and cultured overnight at 5% CO_2, 37°C. SHSY-5Y Control and MECP2 KO cells were seeded at 40 000 cells per well on poly-l-lysine coated plates and incubated in 200 μl differentiation media (above) for

3 days at 5% CO_2, 37°C. On the day of the experiment, the Lucid O_2 platinum sensing probe array and Resipher device (Lucid Scientific, Inc) were pre-warmed in the 37°C incubator. In the 96-well cell plate, 75% of culture media was replaced with fresh pre-warmed growth media (HAP1) or differentiation media (SHSY5Y), the sensing probes were placed in the wells, and Resipher device was attached to the sensing probes. Resipher Oxygen Consumption calculations were gathered for over at least 48 h in a 5% CO_2, 37°C environment at which point rotenone and antimycin A were added to the wells at a concentration of 1 μM. In order to account for cell replication, cell plates were made in triplicate and cell counts or protein concentrations were taken from these replicate plates when the Resipher experiment started, approximately 24 h into the experiment, when rotenone/antimycin were added and/or from the actual Resipher experiment plate at the end of the experiment. Cell counts were made in HAP1 cell plates by removing culture media, adding 10 mM EDTA in PBS to release cells from the plate, incubating on a rocker at 4°C for 10 min, and taking counts from cells suspended in solution. Protein concentration was determined in SHSY5Y cell wells by removing culture media, washing three times with PBS containing 0.1 mM $CaCl_2$ and 1.0 mM $MgCl_2$, and using the Pierce BCA Assay Kit (Thermo Scientific, Cat# 23227) according to manufactures specifications. Absorbance was read on a Biotek plate reader with Biotek Gen5 software. Estimated cell numbers were calculated deriving the doubling time using the formula $N_t = N_0 2\exp(t/T_d)$ where N_0 is the initial cell number, N_t is the cell number at time t and T_d is the doubling time. To assess the effect of genotype on respiration and cell number we integrated the area under the curve using Prism Version 10.0.1 (170).

Cell lysis, SDS-PAGE, western blotting, and silver stain

For cellular lysis, cells were cultured as above, washed twice in phosphate buffered saline (Corning 21-040-CV) containing 0.1 mM $CaCl_2$ and 1.0 mM $MgCl_2$ and lysed in 8M urea with Complete protease inhibitor (Roche 11245200) and/or Halt phosphatase inhibitor (Pierce A32957) and incubated on ice for 30 min. Lysis was sonicated for 10 short bursts at 20% amplitude to shear DNA. Lysis was then centrifuged at 20 000 g for 10 min at 4°C to clarify any insolubilized tissue. Total protein content was determined by Bradford (BioRad 5000006) or BCA (Pierce 23227) assays as per manufactures' protocols. For SDS-PAGE, lysis was reduced and denatured in Laemmli buffer containing SDS and 2-mercaptoethanol and heated for 5 min at 75°C. Equal micrograms of samples were loaded onto 4–20% Criterion gels (BioRad 5671094) for electrophoresis and used for silver staining or transferred to PVDF (Millipore IPFL00010) using the semi-dry transfer method for western blotting. For silver stain, gels were fixed overnight in 50% methanol, 12% acetic acid, and 0.02% formalin. The following day the gel was washed three times, 20 min each, with 50% ethanol followed by 1-min soak in 2 mM sodium thiosulfate. Gels were then washed again with three quick washes in water and soaked in a 12 mM silver nitrate, 0.03% formalin solution for 20 min. After another 2 quick washes, gel was developed in 1.2% sodium carbonate, 0.004% formalin, 7.6 mM sodium thiosulfate. For western blots, membranes were blocked in Tris buffered saline containing 0.05% Triton X-100 (TBST) and 5% non-fat milk for 30 min at room temperature. Membranes were then rinsed of blocking solution and incubated overnight with primary antibody diluted in antibody base solution (PBS, 3% bovine serum albumin, 0.2% sodium azide). Membranes were washed in TBST. HRP conjugated secondary antibodies were diluted 1:5000 in blocking solution and incubated with membranes for 30 min at room temperature. Washed membranes were then exposed to Amersham Hyperfilm ECL (GE Healthcare 28906839) with Western Lightning Plus ECL reagent (Perkin Elmer NEL105001EA). Densitometry was quantified with Fiji Image J software.

Primary Antibodies: MPC1 1:250 (Sigma HPA045119), MPC2 1:500 (Protein Tech Group 20049-1-AP), SLC25A1 1:500 (Protein Tech Group 15235-1-AP), MECP2 1:500 (Invitrogen PA-1-888), Actb 1:500 (Sigma, A5451), GFP 1:1000 (Synaptic Systems 132002).

Secondary Antibodies: HRP anti Mouse 1:5000 (Invitrogen A10668), HRP anti rabbit 1:5000 (Invitrogen G21234).

Immunoprecipitation

For immunoprecipitation, Dynabeads Sheep anti-Mouse IgG (Invitrogen 11031) magnetic beads (30 μl) were incubated at room temperature for 2 h with 1 μg mouse monoclonal anti-GFP (Invitrogen 3E6 A-11120), washed thrice with Wash Buffer (150 mM NaCl, 10 mM HEPES, 1 mM EGTA, and 0.1 mM $MgCl_2$, pH 7.4 with 0.1% Triton X-100) and then incubated with 350 μg protein in 1:1 8 M urea with Complete protease inhibitor (Roche 11245200) sample lysis:Buffer A/0.5% Triton X-100 (150 mM NaCl, 10 mM HEPES, 1 mM EGTA, and 0.1 mM $MgCl_2$, with 0.5% Triton X-100 and Complete protease inhibitor (Roche 11245200)). After sample had incubated with beads for 4 h at 4°C, the beads were washed 6 times with Wash Buffer, and proteins eluted from beads with Laemmli buffer. Samples were then resolved by SDS-PAGE followed by western blot as described above.

RNAseq

Trizol RNA extraction, library construction, and sequencing were performed by BGI. Quality control of total RNA quality and quantity was done on the Agilent 2100 Bio analyzer (Agilent RNA 6000 Nano Kit, Cat# 5067-1511) QC: RNA concentration, RIN value, 28S/18S and the fragment length distribution. For library generation, poly-T oligo-attached magnetic beads were used to isolate poly-A containing mRNAs. Poly-A mRNA was fragmented using divalent cations under elevated temperature. RNA fragments were copied into first strand cDNA with reverse transcriptase and random primers. Second strand cDNA synthesis was done using DNA Polymerase I and RNase H. cDNA fragments underwent addition of a single 'A' base followed by ligation of the adapter. The products were isolated and enriched by PCR amplification. PCR yield was quantified by Qubit. Samples were pooled together to make a single strand DNA circle, giving the final library. DNA nanoballs were generated with the single strand DNA circle by rolling circle replication to increase fluorescent signals during sequencing. DNA nanoballs were loaded into the patterned nanoarrays. Pair-end reads of 100 bp were read on a BGISEQ-500 platform for data analysis. The BGISEQ-500 platform combined the DNA nanoball-based nanoarrays and stepwise sequencing using Combinational Probe-Anchor Synthesis Sequencing Method.

For sequencing analysis, FastQC was used to remove samples of poor quality [19]. We then used the usegalaxy.org server where we were uploaded sequencing reads for analysis [20]. The Galaxy server (v. 21.01) running Hisat2 (Galaxy Version 2.1.0 + galaxy7), FeatureCounts (Galaxy Version 2.0.1), and Deseq2 (Galaxy Version 2.11.40.6 + galaxy1) was used to map sequence reads [21–23]. FeatureCounts files and raw files are available at GEO with accession GSE140054 and compiled file is GSE140054_AllTissueFeatureCounts.txt.gz. In order to determine differential expression, the DESeq2 package was used [23]. We

did not change the default settings and thus the statistics on determining differential expression are well outlined in: https://hbctraining.github.io/DGE_workshop_salmon/lessons/05_DGE_DESeq2_analysis2.html Default was used to estimate size factors (for normalization):" "ratio" uses the standard median ratio method introduced in DESeq. The size factor is the median ratio of the sample over a "pseudosample": for each gene, the geometric mean of all samples. We did not do any pre-filtering of zeros across conditions. For differential expression, we stuck with the default parametric fit type because it is less sensitive to a single sample that may have a large count relative to all the other samples with low counts. And we saw decreasing gene-wise dispersion estimates over the mean; thus, a parametric fit was used for comparing expression levels. Our adjusted p-value was calculated using with the Benjamini-Hochberg procedure controlling for the false discovery rate (FDR). Because we had more than 2 replicates per condition, DESeq2 automatically filtered genes which contain a Cook's distance above a cutoff that is determined based on sample size and number of parameters needing to be estimated. The default cutoff determined by "the 99% quantile of the F(p,m-p) distribution (with p the number of parameters including the intercept and m number of samples). (http://bioconductor.org/packages/devel/bioc/vignettes/DESeq2/inst/doc/DESeq2.html#multi-factor-designs). DESeq2 performs independent filtering by default using the mean of normalized counts as a filter statistic. Meaning it filtered out genes unlikely to produce low p-values. Thus prior to multiple testing corrections and Wald Testing (hypothesis testing) those genes with low counts (zeros) and outliers are removed (given NA values) and then those unlikely have low p-values become NA in adj-P value column. Variance-stabilized normalized counts and regularized log-transformed counts were also generated because they were preferred for any downstream clustering or visualization. We utilized Hisat2 with the following settings: paired-end, unstranded, default settings (except for when a GTF file was used for transcript assembly). For GTF files, we used the *Mus musculus* (Mouse), Ensembl, GRCm38 build from iGenome (Illumina). The aligned SAM/BAM files were processed using Featurecounts with Default settings except we used Ensembl GRCm38 GTF file and output for DESeq2 and gene length file.

Small RNA profiling

Total RNA was purified from the dissected tissue specimens using the Qiagen miRNeasy kit. After examining RNA quality and yield, stranded libraries were prepared with the Illumina TruSeq Small RNA Library Prep kit with the following modifications to the protocol. First, the final library amplification was done with 15 cycles PCR. Second, the PCR products were pooled into 6 sets of 6 samples each prior to loading on a 4% MetaPhor agarose gel. From these gels, a single band at approximately 150 bp was excised, which was then centrifuged at 14 000 RPM through a Gel Breaker Tube (Ist Engineering). The eluted libraries were then concentrated by ethanol precipitation according to the protocol in the Illumina manual. Libraries were sequenced on an Illumina NextSeq500 instrument with a single-end 50 bp read using 2.0 pM loading concentration with 1% PhiX spike. All Mecp2 tissue samples were run together, without any other samples in the sequencing run. Samples generated an average of 8.13 million reads/sample (SE ±380 033), with average Q scores of 34.66. Reads were aligned to the Mm10 mature miRbase 22 reference database using a seed length of 19 bases, allowing 1 mismatch per seed. An average of 4.30 million (±313 224) alignments/sample were identified, with an average alignment Q score of 34.4. Reads were quantified and filtered to include the 80th percentile of features with the highest minimum count and exclude those with a maximum count <10. The resulting 503 miRNAs were then normalized using the counts per million (CPM) method, and log2 transformed before being subjected to statistical testing and downstream analyses using Qlucore Omics Explorer Version 3.6 [24] using normalized data to a variance of 1 and a mean of 0 followed by t-test comparisons without multiple corrections.

Mouse tissue TMT mass spectroscopy

Each tissue sample was homogenized in 500 μl of 8 M urea/100 mM NaHPO4, pH 8.5 with HALT protease and phosphatase inhibitor cocktail (Pierce 78440) using a Bullet Blender (Next Advance) according to manufacturer protocols. Briefly, tissue lysis was transferred to a 1.5 ml Rino tube (Next Advance) with 750 mg stainless steel beads (0.9–2 mm in diameter) and blended for 5 min intervals, two times, at 4°C. Protein supernatants were sonicated (Sonic Dismembrator, Fisher Scientific) three times for 5 s, with 15 s intervals of rest, at 30% amplitude to disrupt nucleic acids, in 1.5 ml Eppendorf tubes. Protein concentration was determined by BCA method, and aliquots were frozen at −80°C. Protein homogenates (100 μg) were diluted with 50 mM NH4HCO3 to a final concentration of less than 2 M urea and treated with 1 mM dithiothreitol (DTT) at 25°C for 30 min, followed by 5 mM iodoacetimide (IAA) at 25°C for 30 min in the dark. Proteins were digested with 1:100 (w/w) lysyl endopeptidase (Wako) at 25°C for 2 h followed by another overnight digestion with 1:50 (w/w) trypsin (Promega) at 25°C. Resulting peptides were desalted on a Sep-Pak C18 column (Waters) and dried under vacuum.

In order to compare all samples per tissue type, 10 individual samples and one composite sample were labeled using the TMT 11-plex kit (ThermoFisher 90406). Labeling was performed as previously described [25, 26]. Briefly, each sample of 100 μg vacuum desiccated peptides was re-suspended in 100 mM TEAB buffer (100 μl). The TMT labeling reagents were equilibrated to room temperature, and anhydrous ACN (256 μl) was added to each reagent channel. Channels were gently vortexed for 5 min, and then 41 μl from each TMT channel was transferred to the peptide solutions and allowed to incubate for 1 h at room temperature. Reactions were quenched with 5% (v/v) hydroxylamine (8 μl; Pierce). All 10 channels were then combined and dried by SpeedVac (LabConco) to ∼150 μl and diluted with 1 ml of 0.1% (v/v) TFA, followed by acidification to a final concentration of 1% (v/v) FA and 0.1% (v/v) TFA. Peptides were desalted with a 200 mg C18 Sep-Pak column (Waters). Each Sep-Pak column was activated with 3 ml of methanol, washed with 3 ml of 50% (v/v) ACN, and equilibrated with 2 × 3 ml of 0.1% TFA. The samples were then loaded and each column was washed with 2 × 3 ml 0.1% (v/v) TFA, followed by 2 ml of 1% (v/v) FA. Elution was performed with 2 volumes of 1.5 ml 50% (v/v) ACN. Eluates were dried to completeness.

High pH fractionation was performed essentially as described with slight modification [25]. Dried samples were re-suspended in high pH loading buffer (0.07% v/v NH4OH, 0.045% v/v FA, 2% v/v ACN) and loaded onto an Agilent ZORBAX 300 Extend-C18 column (2.1 × 150 mm with 3.5-μm beads). An Agilent 1100 HPLC system was used to carry out the fractionation. Solvent A consisted of 0.0175% (v/v) NH4OH, 0.0125% (v/v) FA, and 2% (v/v) ACN; solvent B consisted of 0.0175% (v/v) NH4OH, 0.0125% (v/v) FA, and 90% (v/v) ACN. The sample elution was performed over a 58.6-min gradient with a flow rate of 0.4 ml/min. The gradient consisted of 100% solvent A for 2 min, 0–12% solvent B over 6 min, 12–40%

over 28 min, 40–44% over 4 min, 44–60% over 5 min, and then held constant at 60% solvent B for 13.6 min. A total of 96 equal volume fractions were collected across the gradient, pooled by concatenation into 24 fractions, and dried to completeness using a vacuum centrifugation.

Each of the 24 high-pH peptide fractions was resuspended in loading buffer (0.1% FA, 0.03% TFA, 1% ACN). Peptide eluents were separated on a self-packed C18 (1.9 μm Maisch) fused silica column [25 cm × 75 μm internal diameter (ID), New Objective] by an Easy nLC 1200 (Thermo Scientific) and monitored on a Q-Exactive HFX MS (Thermo Scientific). Elution was performed over a 120-min gradient at a rate of 300 nl/min with buffer B ranging from 3% to 40% (buffer A: 0.1% FA in water; buffer B: 0.1% FA in 80% ACN). The mass spectrometer acquired data in positive ion mode using data-dependent acquisition with top 10 cycles. Each cycle consisted of one full MS scan followed by a maximum of 10 MS/MS. Full MS scans were collected at a resolution of 120 000 (400–1600 m/z range, 3 × 106 AGC, 100 ms maximum ion injection time). Higher energy collision-induced dissociation (HCD) MS/MS spectra were acquired at a resolution of 45 000 (1.6 m/z isolation width, 30% collision energy, 1 × 10–5 AGC target, 86-ms maximum ion time). Dynamic exclusion was set to exclude previously sequenced peaks for 20 s within a 10-ppm isolation window.

Raw TMT files were searched using Thermo's Proteome Discoverer suite (version 2.1.1.21) with Sequest HT. The spectra were searched against a mouse Uniprot database downloaded July, 2018 (98 225 target sequences). Search parameters included 20 ppm precursor mass window, 0.05 Da product mass window, dynamic modifications methione (+15.995 Da), deamidated asparagine and glutamine (+0.984 Da), phosphorylated serine, threonine and tyrosine (+79.966 Da), and static modifications for carbamidomethyl cysteines (+57.021 Da) and N-terminal and lysine-tagged TMT (+229.26340 Da). Percolator was used filter PSMs to 0.1%. Peptides were grouped using strict parsimony and only razor and unique peptides were used for protein level quantitation. Reporter ions were quantified from MS2 scans using an integration tolerance of 20 ppm with the most confident centroid setting. Only unique and razor (i.e. parsimonious) peptides were considered for quantification. Volcano plot p values were calculated using Qlucore Omics Explorer Version 3.6 [24]. Data were normalized to a variance of 1 and a mean of 0 followed by t-test comparisons without multiple corrections.

Cell lines TMT mass spectrometry

Cells were washed three time with ice cold PBS and detached from plates by incubation with ice cold PBS plus 10 mM EDTA. Cells were pelleted at 1000 × g for 5 min at 4°C and cell pellets were flash frozen in liquid nitrogen and stored at −80°C. Cell pellets were lysed in 8 M urea, 50 mM Tris HCl, pH 8.0, 1× Roche Complete Protease Inhibitor and 1× Roche PhosStop. Lysates were quantified by Qubit fluorometry (Life Technologies). Samples were digestion overnight with trypsin. Briefly, sample reduction was done for 1 h at RT in 12 mM DTT followed by alkylation for 1 h at RT in 15 mM iodoacetamide. Trypsin was added at an enzyme:sample ratio of 1:20. Each sample was acidified in formic acid and subjected to SPE on an Empore SD C18 plate. For TMT labeling, after trypsin digestion ach sample was acidified in formic acid and subjected to SPE on an Empore SD C18 plate (3 M catalogue# 6015 SD). Samples were dried out/lyophilized and reconstituted in 140 mM HEPES, pH 8.0, 30% acetonitrile. Fourty μl of acetonitrile was added to each TMT tag tube and mixed extensively. Tags were incubated at room temperature for 15 min. 30 μl of label was added to each peptide sample and mixed aggressively. Samples were incubated in an Eppendorf Thermomixer at 300 rpm 25°C for 1.5 h. Reactions were terminated by adding 8 μl of fresh 5% hydroxylamine solution and 15 min incubation at room temperature. Samples underwent high pH reverse phase fractionation following this conditions; Buffers: Buffer A: 10 mM NaOH, pH 10.5, in water Buffer B: 10 mM NaOH, pH 10.5, in acetonitrile. We used XBridge C18 columns, 2.1 mm ID × 150 mm length, 3.5 μm particle size (Waters, part #186003023) hooked up to an Agilent 1100 HPLC system equipped with a 150 μl sample loop operating at 0.3 ml/min, detector set at 214 nm wavelength. Dried peptides were resolubilized in 150 μl of Buffer A and injected manually. Fractions were collected every 30 s from 1–49 min (96 fractions total, 150 μl/fraction). We analyzed by mass spectrometry 10% per pool for the full proteome in a nano LC/MS/MS with a Waters NanoAcquity HPLC system interfaced to a ThermoFisher Fusion Lumos mass spectrometer. Peptides were loaded on a trapping column and eluted over a 75 μm analytical column at 350 nl/min; both columns were packed with Luna C18 resin (Phenomenex). Each high pH RP fraction was separated over a 2 h gradient (24 h instrument time total). The mass spectrometer was operated in data-dependent mode, with MS and MS/MS performed in the Orbitrap at 60 000 FWHM resolution and 50 000 FWHM resolution, respectively. A 3 s cycle time was employed for all steps. Data Processing Data were processed through the MaxQuant software v1.6.2.3. Data were searched using Andromeda with the following parameters: Enzyme: Trypsin Database: Uniprot Rat, Fixed modification: Carbamidomethyl (C) Variable modifications: Oxidation (M), Acetyl (Protein N-term), Phopho (STY; PO4 data only). Fragment Mass Tolerance: 20 ppm. Pertinent MaxQuant settings were: Peptide FDR 0.01 Protein FDR 0.01 Min. peptide Length 7 Min. razor + unique peptides 1 Min. unique peptides 0 Second Peptides FALSE Match Between Runs FALSE The protein Groups.txt files were uploaded to Perseus v1.5.5.3 for data processing and analysis.

For phosphopeptide enrichment, we used two buffers Buffer A: 200 μl of solution A + 800 μl of acetonitrile/0.4% TFA and buffer B consisting of lactic Acid, 300 mg/ml in Buffer A. Dried peptides were resuspended in 100 μl of buffer B. TiO2 tips (TiO2 enrichment kit, GL Sciences part # 5010-21312) were pre-washed/equilibrated with 20 μl of buffer A, spun at 3000 × g for 2 min, followed by 20 μl of buffer B, spin at 3000 × g for 2 min. Samples were loaded onto a TiO2 tip, spun at 500 × g for 2 min. Flow through underwent loading onto a TiO2 tip, spun at 500 × g for 2 min. Samples were washed with 20 μl of buffer B, spun at 3000 × g for 2 min followed by 2 × 20 μL of buffer A, spun at 3000 × g for 2 min. Peptides were eluted with 50 μl of 5% NH4OH (pH 11.0) solution, followed by 50 μl of 5% Pryrrolidine (pH 12.0). Eluates were frozen, dried in a lyophilizer and resuspended in 0.1% TFA for analysis.

Stable isotope tracing experiments

250 000 cells per well were plated on a 6-well plate in 2 ml of DMEM (25 mM glucose, no pyruvate, penicillin/streptomycin, and 10% FBS). The next day, the cells were washed in 2 ml of PBS and 2 ml of DMEM media DMEM (25 mM glucose, no pyruvate, penicillin/streptomycin, and 10% dialyzed FBS) containing 1 mM $^{13}C_3$ Pyruvate was added. After 12 h, the medium was aspirated and 400 μl of lysis buffer (0.1 M formic acid at 4:4:2 dilution (MeOH: ACN: Water)) was added. After 2 min on ice, 35 μl of 15% NH_4HCO_3 was added and incubated for another 20 min on ice. Cells were then scraped, and lysates were transferred into pre-chilled 1.5 ml centrifuge tubes, vortexed briefly, and spun at 15 060 rpm. For 30 min at 4°C. 390 μl of supernatant were

then transferred into pre-chilled 1.5 ml centrifuge tubes and dried down using a Savant Speedvac Plus vacuum concentrator. Samples were resuspended in 120 μl of 4:1 (ACN: Water), sonicated for 5 min at 4°C, and centrifuged at 15 060 r.p.m. for 20 min at 4°C. 100 μl of supernatant was transferred into a pre-chilled LC-MS vial. 5 μl of this sample was injected on a HILIC-Z column (Agilent Technologies) and ^{13}C labeled TCA intermediates were measured on an Agilent 6546 QTOF mass spectrometer that was coupled with an Agilent 1290 Infinity II UHPLC system (Agilent Technologies). The column temperature was maintained at 15°C and the autosampler was at 4°C. Mobile phase A: 20 mM Ammonium Acetate, pH = 9.3 with 5 μM Medronic acid, and mobile phase B: acetonitrile. The gradient run at a flow rate of 0.4 ml/min was: 0 min: 90% B, 1 min 90% B, 8 min: 78% B, 12 min: 60% B, 15 min: 10% B, 18 min: 10%B, 19-23 min: 90% B. The MS data were collected in the negative mode within an m/z = 20-1100 at 1 spectrum/sec, Gas temperature: 225°C, Drying Gas: 9 l/min, Nebulizer: 10 psi, Sheath gas temp: 375°C, Sheath Gas flow: 12 l/min, VCap: 3000 V, Nozzle voltage 500 V, Fragmentor: 100 V, and Skimmer: 45 V. Data were analyzed using Masshunter Qualitative Analysis 10 and Profinder 10 (Agilent Technologies).

Bioinformatic analyses

Gene ontology studies were performed with Cluego and Metascape. ClueGo v2.58 run on Cytoscape v3.8.2 [27, 28]. ClueGo was done querying GO CC and REACTOME, considering all evidence at a Medium Level of Network Specificity and selecting pathways with a Bonferroni corrected p value <10E−3. ClueGo was run with Go Term Fusion. To compare ontologies, we selected Metascape under multiple gene list and express analysis settings [29]. Analysis of microRNA targets was performed with the web tool MIENTURNET. High confidence network of targets was filtered using as parameters miRNA target interactions threshold at 2, FDR <0.06, cumulative weighted context++ score at 0.85, and probability of conserved targeting at 0.6 [30].

Statistical analyses

Volcano plot p values were calculated using Qlucore Omics Explorer Version 3.6 [24] without multiple corrections. Statistical analyses were performed with the engine https://www.estimationstats.com/#/ with a two-sided permutation t-test and alpha of 0.05 [31]. Other statistical analyses were performed with Prism v9.5.0(525).

Results

Organ-specific divergence of the *Mecp2* mutant transcriptomes and proteomes

Bulk transcriptome and proteome analyses of microdissected brain regions (cortex, hippocampus, striatum), liver, kidney, and skeletal muscle from wild type and *Mecp2*$^{tm1.1Bird/y}$ mice were analyzed to define systemic molecular phenotypes in *Mecp2*-null mice. To define molecular changes preceding overt disease, mutant mice were sacrificed at 45 days of age. Approximately 80% of *Mecp2*$^{tm1.1Bird/y}$ mice survive to this age, fifty percent of the mice are neurologically symptom-free, and there is no overt organ pathology, such as fatty liver [32].

The *Mecp2*-null mutation affected the transcriptome of all tissues analyzed (Fig. 1A and B). The top-ten most increased or decreased transcripts differed across tissues (Fig. 1B). Whole transcriptomes segregated organs and brain regions by genotype as revealed by Uniform Manifold Approximation and Projection analysis (Fig. 1C, UMAP). Each one of the *Mecp2*$^{tm1.1Bird/y}$ tissues analyzed had a similar percentage of transcripts with either increased or decreased steady-state levels (Fig. 1A, red and blue symbols respectively). However, the total number and identity of differentially expressed transcripts varied among these tissues (Fig. 1A and B). The most affected tissues were liver and kidney, with ∼7–8% of all quantified mRNAs with steady-state levels modified by the *Mecp2* mutation (Fig. 1A). In contrast, microdissected brain regions were the least affected tissues, with altered expression of 1.4–4.4% of the mRNAs (Fig. 1A). Transcriptome similarity matrices comparing across brain regions and genotypes showed that the *Mecp2*$^{tm1.1Bird/y}$ mutation caused the most pronounced differences between genotypes in cortex as compared to hippocampus and striatum (Fig. 1D). We chose the *Mecp2*$^{tm1.1Bird/y}$ cortical transcriptome to determine its replicability. The Pearson correlation among *Mecp2*$^{tm1.1Bird/y}$ differentially expressed mRNAs was 0.68 in two independent cohorts of microdissected cortices and transcriptional analyses (Fig. 1E). A similar correlation was obtained comparing our findings with either public whole-cell or nuclear cortical transcriptome datasets obtained in the same *Mecp2*$^{tm1.1Bird/y}$ mouse at a similar age (Fig. 1F and G, Pearson = 0.69 and 0.59) [33]. We previously validated mRNA steady-state differences across wild type brain regions against Allen mouse brain transcriptome data (r = 0.69) [34]. These multipronged validation approaches show that our bulk transcriptome data fulfill reproducibility standards.

Since the *Mecp2* mutation alters the transcriptome across all organs, pathway analysis were performed using whole tissue transcriptomes and the Gene Set Enrichment Analysis (GSEA) tool [35] to identify processes/mechanisms commonly affected across the different tissues. These analyses did not identify significant pathways shared across mutant tissue transcriptomes (data not shown). We therefore focused on *Mecp2*-sensitive mRNAs shared by all tissues to define common pathway phenotypes. The expression of 20 mRNAs was altered by the *Mecp2* mutation in all tissues (Supplementary Fig. S1A). The overlap among brain regions was also discrete with 69 differentially expressed mRNAs whose levels were modified in all three brain regions. Of these 69 overlapping brain mRNAs, 38 were identified as congruently changed in independent cortical datasets listed above (Supplementary Fig. S1B, bold red and blue fonts). These 69 differentially expressed mRNAs were not enriched in significant ontologies or pathways. Thus, *Mecp2* mutations alter the transcriptome systemically with minimal transcript overlap across tissues, and no apparent pathway enrichment in brain or other tissues.

The performance of the transcriptome to identify systemic pathways sensitive to *Mecp2* gene defects prompted us to ask whether the proteome could better predict pathways affected by *Mecp2* mutations. The proteome was assessed using Tandem Mass Tagging (TMT) quantitative mass spectrometry of microdissected brain regions, liver, and skeletal muscle to measure the extent of the *Mecp2*-sensitive proteome (Fig. 2A) [36]. A total of 10 087 proteins were simultaneously quantified across these tissues in both genotypes; corresponding to 5332 in cortex, 5540 in hippocampus, 2874 in striatum, 8579 in liver, and 5842 proteins in skeletal muscle. In distinct contrast to the transcriptome, the cortex proteome was the most affected tissue with the steady-state levels of 322 proteins, 6% of the quantified cortex proteome, altered in *Mecp2* mutants (Fig. 2A and B). Liver and skeletal muscle proteomes were moderately affected with 130 (1.5%) and 167 (3.2%) protein levels altered, respectively (Fig. 2A and B). In contrast, the proteomes of hippocampi and striata were minimally disrupted by the *Mecp2* mutation (Fig. 2A and B). Divergences between the tissue transcriptomes and proteomes

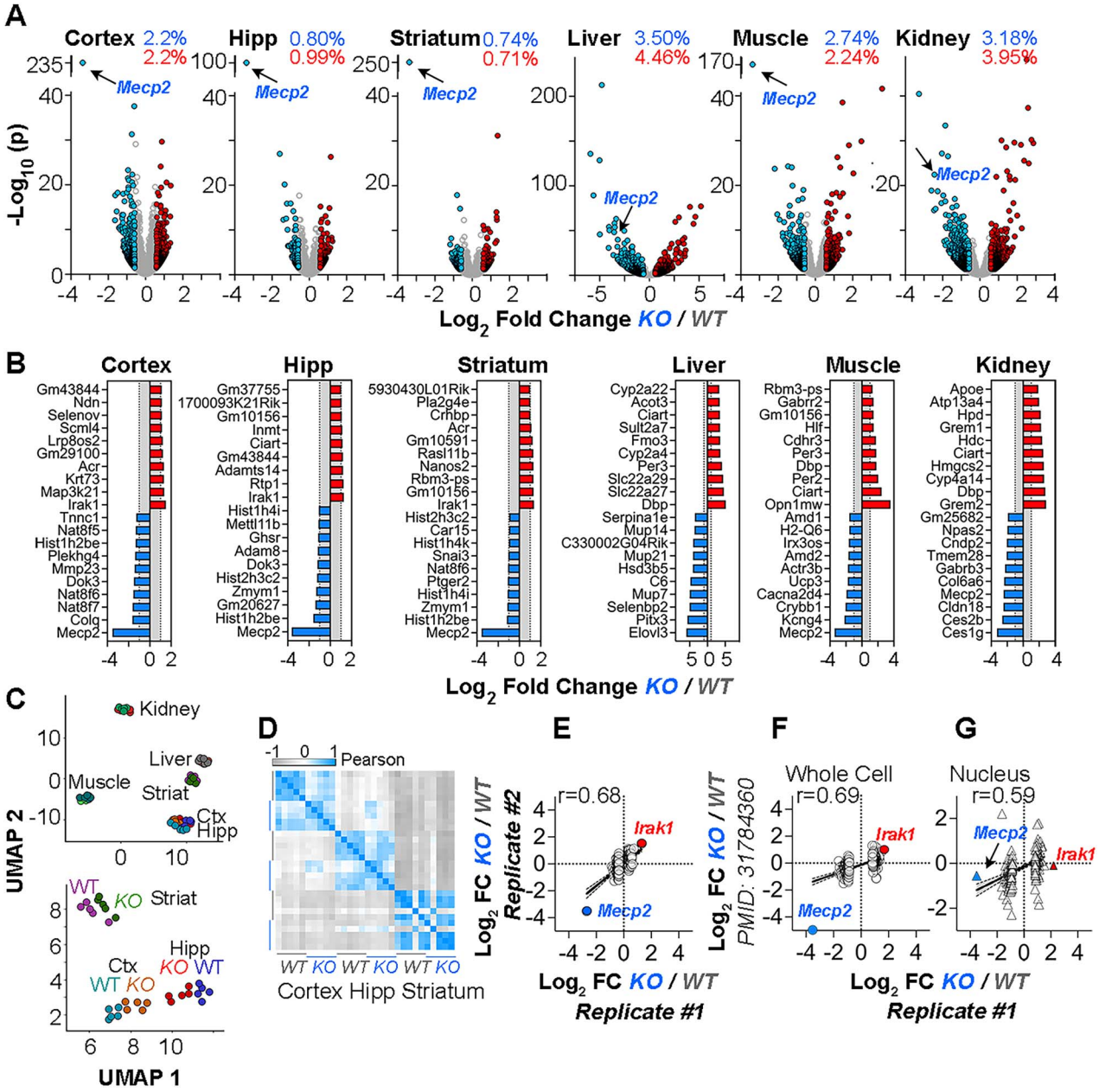

Figure 1. The *Mecp2*$^{tm1.1Bird/y}$ tissue-specific transcriptomes. (A) Volcano plots of microdissected cortex, hippocampus, striatum, liver, skeletal muscle, and kidney. Fold of change threshold is 1.5-fold and corrected p value cut-off is set at 0.05. Symbols to the right and left represent transcripts whose steady-state levels are increased and decreased in mutants, respectively (n = 5 animals of each genotype). (B) Top 10 most increased and decreased transcripts in *Mecp2* null tissues. Data expressed as log2 fold of change. Gray area depicts the −1 to +1 log2 interval. (C) UMAP analysis wild type and mutant tissue whole transcriptomes. (D) Pearson correlation similarity matrix of wild type and mutant microdissected brain regions whole transcriptomes. (E) Pearson correlation of two independent microdissected cortical transcriptome datasets (n = 5 animals of each genotype per dataset). (F, G) Pearson correlation of microdissected cortical transcriptome Replicate #1 with bulk cortical tissue or nuclear fraction transcriptomes reported by Clemens *et al.* [33]. This dataset was chosen because of the age, the use of the *Mecp2*$^{tm1.1Bird/y}$ mouse strain, and brain region analyzed match those used by us. The top 100 most increased and decreased transcripts in the Replicate #1 mutant dataset were compared with Replicate #2 in E and with Clemens *et al.* datasets in F-G. The two most changed transcripts *Mecp2* and *Irak1* are antipodes shared by all datasets. Datasets available in supplementary table 2.

prompted us to assess the similarity of the transcriptome and proteome across tissues (Fig. 2C). Steady-state level differences from all significantly changed *Mecp2*-sensitive transcripts were compared to the corresponding protein levels. Although the proteome and transcriptome correlated in wild type cortex (Fig. 2D, r = 0.38), the *Mecp2*-sensitive cortical transcriptome-proteome (encompassing 1532 mRNA-protein pair quantifications) did not correlate (Fig. 2C, r = 0.0058). The lack of correlation in mutant cortex is in stark contrast with the correlation between the liver *Mecp2*-sensitive transcriptome and proteome, where the Pearson correlation was 0.69 for a large size set of transcript-protein pairs (Fig. 2C, n = 767 pairs), a value comparable to the correlation between the liver proteome and transcriptome in wild type tissue (Fig. 2D, r = 0.50). We hypothesized that differences in the expression of small regulatory microRNAs could account for divergent correlations between the proteome and the transcriptome in cortex and liver of *Mecp2*$^{tm1.1Bird/y}$ animals (Supplementary Fig. S2). However, the number of microRNAs

differentially expressed in these *Mecp2* mutant tissues and their predicted target mRNAs is unlikely to account for the poor correlation of the transcriptome and proteome in *Mecp2* mutant cortex. There were few exceptions, such as Slc25a51, a mitochondrial nicotinamide adenine dinucleotide (NAD^+) transporter [37], which is a predicted target of miR-182-5p, a microRNA increased in the microdissected cortex of mutant mice (Supplementary Fig. S2). These results demonstrate that factors other than the transcriptome specify the steady-state proteome in *Mecp2*$^{tm1.1Bird/y}$ brain.

In order to identify universal proteome phenotypes, we focused on proteins that were altered across multiple *Mecp2* mutant tissues. There was minimal overlap among differentially expressed proteins across *Mecp2* mutant brain regions (Fig. 2A, B, E, and Supplementary Fig. S3A), as well as between brain regions and other tissues (Fig. 2B, E and Supplementary Fig. S3A). For example, the mutant cortex and hippocampus shared Mecp2 and two other proteins, cathepsin B (Ctsb) and the mitochondrial complex I assembly factor PreY (Pyurf) [38, 39]. However, levels of these two proteins were affected in opposite directions in microdissected cortex as compared to hippocampus (Fig. 2A, B, E). Other than Mecp2, a single protein was decreased in all tissues the alpha-1-antitrypsin isoform Serpina1e (Fig. 2E and Supplementary Fig. S3A). Serpina1e was in lowest abundance quartile of the *Mecp2*-sensitive cortex proteins while it was in the uppermost quartile in liver and muscle (Supplementary Fig. S3B). Of note, Serpina1e protein levels were previously reported to be reduced in the CSF of *Mecp2* mutant mice [40]. Genetic defects in *Mecp2* cause widespread non-overlapping modifications of the transcriptome and proteome across tissues. Furthermore, the levels of a *Mecp2*-sensitive mRNA variably correlate with the corresponding protein level in tissues with the exception of nervous tissue, where there was no correlation.

Mecp2/MECP2 mutant transcriptomes and proteomes enrich metabolic ontologies across organs and cells

Despite the lack of correlation across tissue transcriptomes, we reasoned that combining *Mecp2* mutant tissue proteomes and transcriptomes may enable identification of shared pathways. *Mecp2*-sensitive proteomes were analyzed with the ClueGo tool and transcriptomes and proteomes were interrogated for pathway convergence with the Metascape tool [27, 29]. Metascape analysis of parental ontologies for tissue transcriptomes and proteomes identified shared ontologies for metabolic process (GO:0008152, Supplementary Fig. S4A) and response to stimulus (GO:0050896, Supplementary Fig. S4A). These parental ontology nodes gave rise to descendant terms with different degrees of representation across tissues and "omic" datasets (Supplementary Fig. S4B). For example, organic hydroxy compound metabolism was represented in all but one of the tissue omics and this term co-clustered with other metabolic ontologies including small molecule catabolic process (GO:0044282 $-\log_{10}$ p value 31.963) and metabolism of lipids (Supplementary Fig. S4B, R-HSA-556833 $-\log_{10}$ p value 55.139). A similar outcome was obtained by interrogating tissue proteomes with the ClueGO tool (Supplementary Fig. S4C). The strongest ontologies were cell responses to stimuli, synaptic, lipid metabolism, mitochondria, and peroxisomes (Supplementary Fig. S4C). These ontologies were represented in all tissue proteomes to a different extent (Supplementary Fig. S4D). Lipid metabolism ontologies preferentially enriched in liver while synaptic and mitochondrial ontologies were enriched in brain (Supplementary Fig. S4C and D). In fact, we found a decreased steady-state level of 10 enzymes required for cholesterol synthesis in *Mecp2*-null liver (Supplementary Fig. S5). Brain and liver proteomes also shared large numbers of synapse-annotated (SynGO), lipid (GO:0006629), and mitochondrial (Mitocarta 3.0) annotated proteins (Supplementary Fig. S4E) [41, 42]. The degree of enrichment in synaptic and mitochondrial annotated proteins in *Mecp2* mutant brains was similarly significant with a 2.4-2.8-fold enrichment (Supplementary Fig. S4F, $p < 2E{-}8$, Exact hypergeometric probability). Similar results were identified analyzing a published *Mecp2* mutant proteome obtained from the whole isocortex of the alternate null allele (*Mecp2* $^{Jae/y}$) at a later, symptomatic, age (P60, Supplementary Fig. S6A and B) [43].

We next asked whether metabolic ontologies found in mouse *Mecp2* mutant tissue proteomes were a universal feature of *MECP2* mutants irrespective of the biological systems scrutinized. We performed TMT quantitative mass spectrometry across human *MECP2*-null cells and their isogenic controls (Fig. 3). The variability between biological replicates from wild type and *MECP2*-null iPSC-derived human neurons was too large to permit identification of *MECP2*-sensitive proteomes in these cells (unpublished data). We therefore analyzed three alternative human cell lines; the chronic myelogenous leukemia male cell line HAP1; and two neuronal female cell lines, LUHMES postmitotic neurons (LUHMES, Lund human mesencephalic neurons), and the SH-SY5Y neuroblastoma cells [24, 44, 45]. Cells of the myeloid lineage express MECP2 protein at levels comparable to brain and show alterations of the transcriptome in Rett patients [4, 46, 47]. We quantified 5958 proteins in LUHMES, 8086 proteins in SH-SY5Y, and 6463 proteins in HAP1 cells. These proteomes identified 186, 323, and 106 proteins whose steady-state levels were altered in *MECP2*-null HAP1 (male), LUHMES (female), and SH-SY5Y cells (female), respectively (Fig. 3A and B). Metascape analysis of parental ontologies shared across cell lines and organ proteomes indicated that the strongest shared ontology was metabolic process (Fig. 3C, GO:0008152, $-\log_{10}$ p value 13, 38.1, and 29.5; ΣBrain, HAP1 and liver, respectively). This parental term enclosed multiple mitochondrial and lipid metabolism ontologies. Among these, the two most widely represented ontologies across *Mecp2/MECP2* proteomes were generation of precursor metabolites and energy with 50% mitochondrial annotated proteins (Fig. 3D, GO:0006091 $-\log_{10}$ p value 13, 17.9, and 2.3; ΣBrain, HAP1 and liver, respectively) and nucleobase-containing small molecule metabolic process with 35% mitochondrial annotated proteins (Fig. 3D, GO:0055086 $-\log_{10}$ p value 10, 3.6, and 6.5; ΣBrain, HAP1 and liver, respectively). The HAP1 and mouse brain proteomes were the datasets with the highest number mitochondrial annotated proteins (Mitocarta 3.0, Supplementary Fig. S7A) [42]. We measured the degree of overlap between human cell line and mouse brain mutant proteomes (Supplementary Fig. S7B, Enrichment) and determined that the *MECP2* HAP1 proteome had the highest overlap normalized by dataset size with either the *Mecp2* mouse brain proteome or the Mitocarta 3.0 proteome among the three human cell lines tested. The *MECP2* mutant HAP1 proteome was enriched in *Mecp2* sensitive mouse brain proteins 4.3-times above what was expected by chance (Supplementary Fig. S7B, $p < 5E{-}4$, Exact hypergeometric probability). These results demonstrate that metabolic and mitochondrial ontologies are a common phenotype across diverse *Mecp2/MECP2* deficient biological systems. These results suggest that mitochondrial and metabolic processes are preponderantly disrupted by genetic defects in *MECP2/Mecp2*.

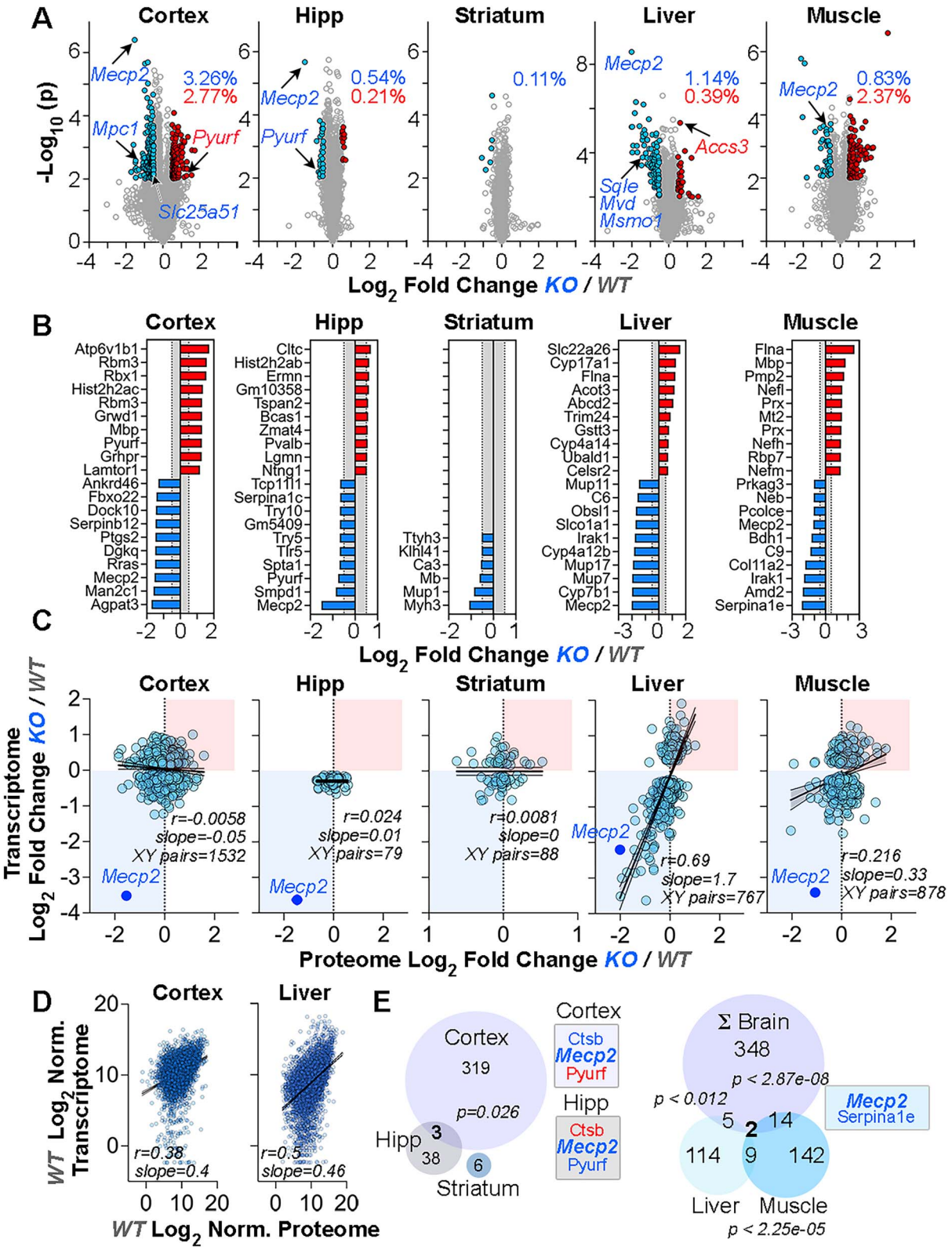

Figure 2. The *Mecp2*$^{tm1.1Bird/y}$ tissue-specific proteomes. (A) Volcano plots of microdissected cortex, hippocampus, striatum, liver, skeletal and muscle. Fold of change threshold is 1.5-fold and p value cut-off is set at 0.05. Symbols to the right and left represent proteins whose steady-state levels are increased and decreased in mutants, respectively (n = 5 animals of each genotype). (B) Top 10 most increased and decreased proteins in *Mecp2* null tissues. Data expressed as log2 fold of change. Gray area depicts the −0.5 to +0.5 log2 interval. (C) Pearson correlation of differentially expressed transcripts thresholded just by corrected p values <0.05 and their matching protein pair for each tissue. (D) Spearman correlation of the whole quantified proteome and transcriptome for microdissected cortex and liver. (E) Venn diagrams of overlapping proteins with altered steady-state levels in mutant brain regions and the sum of all differentially expressed proteins in brain (ΣBrain) compared to muscle and liver mutant proteomes. Hypergeometric p values for the different datasets overlaps. See Supplementary Table S3.

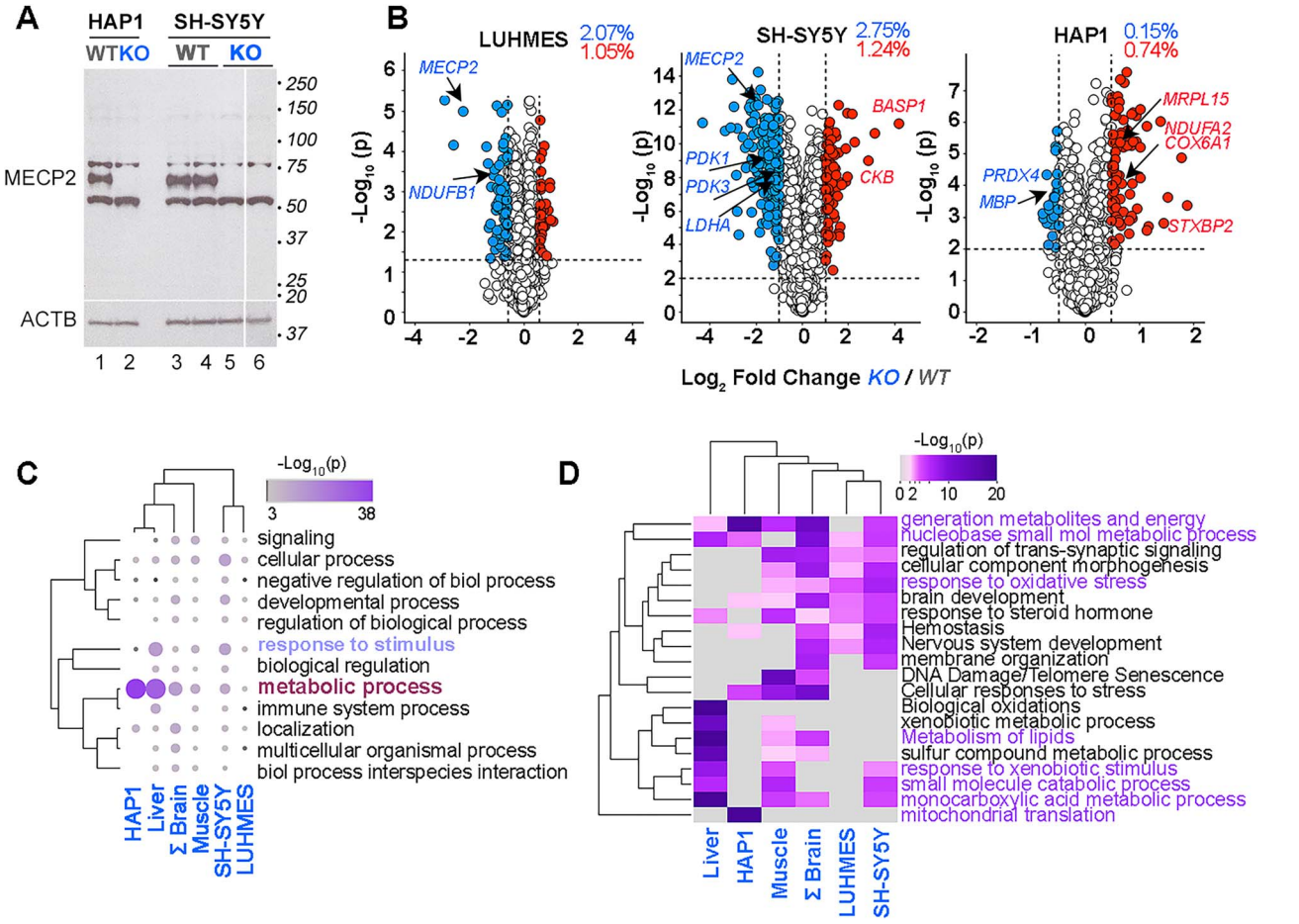

Figure 3. Human cell lines *MECP2* proteomes converge on metabolic and mitochondrial ontologies. (A) Immunoblots of HAP1 and SH-SY5Y cell lines control and *MECP2* edited. Actin B (ACTB) was used as loading control. Lanes 3–4 and 5–6 represent two independent wild type and null cell lines respectively. (B) Volcano plots of LUHMES, SH-SY5Y, and HAP1 wild type and *MECP2*-null cells. Fold of change threshold is 1.5–2-fold and corrected p value cut-off is set at 0.05 for LUHMEs cells, and 0.001 for HAP1 and SH-SY5Y cells. Symbols to the right and left represent proteins whose steady-state levels are increased and decreased in mutants, respectively (n = 5 independent replicates per genotype, except for LUHMEs cells n = 3). (C) Parental GO term ontologies represented in the differentially expressed proteomes of mutant mouse tissues and human cell lines. Clustering performed with Pearson correlation. ΣBrain represents the added microdissected cortex and hippocampal *Mecp2* proteomes. (D) Ontologies, KEGG terms, and pathways enriched and shared by datasets used in C. Accumulative hypergeometric p-values and enrichment factors were calculated and used for filtering. Significant terms were clustered into a tree using kappa-statistical similarities among their gene memberships. Grey denotes no representation of the dataset in an ontology. Datasets available in supplementary tables 4 and 5.

Mecp2/MECP2 mutations differentially disrupt mitochondrial proteins

Mitochondrial annotated proteins intersect synaptic, peroxisome, and lipid metabolism ontologies and processes. Mitochondria occupy 30% of the synapse volume and are necessary for synaptic transmission as well as for cholesterol and fatty acid metabolism [48–52]. Levels of 45 proteins (annotated to Mitocarta 3.0) changed only in cortex including the pyruvate carrier Mpc1, the NAD^+ carrier Slc25a51, and Pyurf (Supplementary Fig. S7C and D) [42]. Coessentiality network analysis with the Fireworks tool (Supplementary Fig. S7D) [53] revealed that the most altered mitochondrial proteins in *Mecp2* mutant cortex, such as Mpc1, Slc25a51, and Pyurf, shared functional relationships with respiratory chain complex I subunits (Supplementary Fig. S7D Pyurf and Ndufab9 nodes) and proteins involved in pyruvate metabolism (Supplementary Fig. S7D Mpc1 node). These results suggest a defect in the mitochondrial pyruvate metabolism.

Mpc1 is necessary for feeding pyruvate into the Krebs cycle, pyruvate incorporation into lipids, for maintaining steady-state levels of fatty acids and cholesterol in cells, and for normal synaptic transmission [54–56]. As such, the Mpc1 pyruvate transporter participates in processes and pathways uncovered by the *Mecp2* mutant proteome pathways and ontologies (Fig. 3C, D and Supplementary Fig. S4C, D). Mpc1 levels were measured by immunoblot in $Mecp2^{tm1.1Bird/y}$ tissues as well as the three human *MECP2* mutant cell lines that we characterized by proteomics (Fig. 4). Mpc1 levels were either decreased or normal in microdissected cortex and hippocampus, respectively (Supplementary Fig. S7C and Fig. 4A, B), thus confirming our mass spectrometry findings (Fig. 2A, B and Supplementary Fig. S7C). Whether changes to levels of Mpc1 in micropunched-dissected tissue are recapitulated in whole isocortex extracts was assessed by immunoblot analysis of whole mouse isocortex extracts (Fig. 4C). The increased levels of Mpc1 in the whole cortex analyses suggests there is heterogeneity among regions of the isocortex (Fig. 4C). Mpc1 levels were increased in liver while Mpc1 and Mpc2 levels were decreased in mutant striated muscle (Fig. 4D and E). These results indicate that steady-state levels of pyruvate carriers are differentially affected in different organs and regionally within the brain.

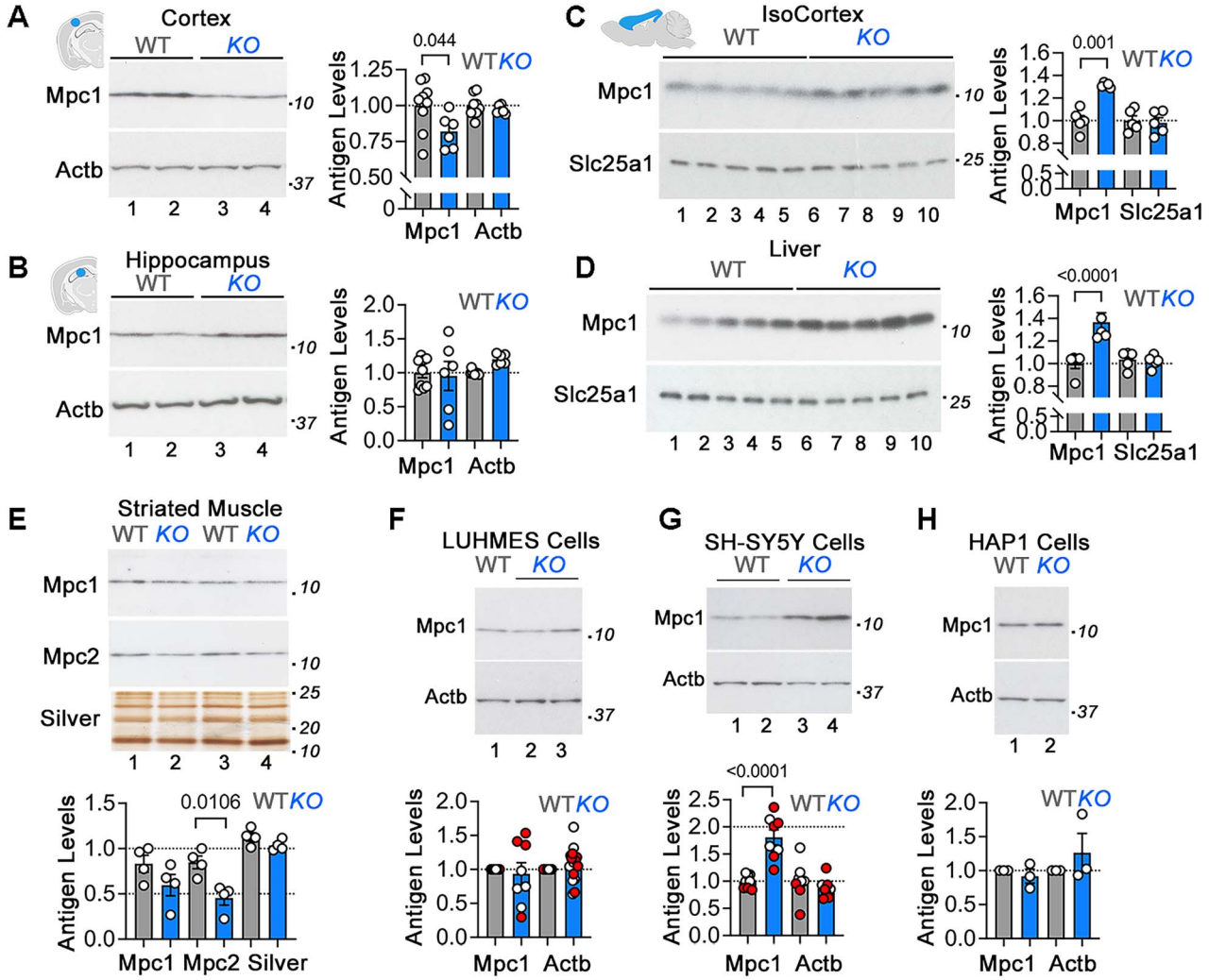

Figure 4. Alterations of mitochondrial pyruvate carrier levels in *Mecp2*$^{tm1.1Bird/y}$ tissues and *MECP2* mutant cells. (A–H) show immunoblots and quantifications of the mitochondrial pyruvate transporters Mpc1 and Mpc2 in *Mecp2*$^{tm1.1Bird/y}$ tissue extracts (A, B, and E), *Mecp2*$^{tm1.1Bird/y}$ total membrane fractions (C and D), and MECP2-null human cell lines (F–H). Loading controls used were beta actin (Actb), the mitochondrial citrate transporter (Slc25a1), or silver stained SDS-PAGE. Quantifications are normalized to wild type antigen levels. Each dot represents an animal or a biological replicate. Dots in F and G depict two independent *MECP2*-null clones. p Values were obtained with two-sided permutation t-test with 5000 bootstrap samples. See Supplementary Table S2.

We then tested whether the variable levels of Mpc1 in mouse mutant tissues could be replicated by *MECP2*-null mutations across different human cell lines (Fig. 4F–H). The expression of Mpc1 in either MECP2 knockout differentiated LUHMES or HAP1 cells was not altered (Fig. 4F and H). In contrast, differentiated SH-SY5Y cells lacking MECP2 had 2-fold increase in Mpc1 expression (Fig. 4G). These finding indicate that *MECP2* mutations alter the expression of mitochondrial proteins and Mpc1 in a tissue and cell type-dependent manner. These findings suggest that *Mecp2*/*MECP2* mutant mitochondrial phenotypes such as respiration and pyruvate consumption may vary across cells and tissues.

Mitochondrial respiration is altered in cells lacking MECP2

Tissue/cell type-specific modifications of the mitochondrial proteome in *Mecp2*/*MECP2*-null tissues and cell lines raise questions about mitochondrial functional phenotypes and the uniformity of these phenotypes across cell types. Mitochondrial respiration was measured in intact cells using Seahorse respirometry in complete media with glucose, pyruvate, and glutamine as carbon sources [57]. We postulated respiration phenotypes could be stunted by the anatomical heterogeneity inherent to primary cultures generated from whole isocortices as seen in the differing levels of Mpc1 between microdissected cortex and isocortex samples (compare Fig. 4A and C). Nevertheless, a discrete but significant decrease in the basal respiratory capacity was observed in primary neuronal cultures prepared from whole *Mecp2*$^{tm1.1Bird/y}$ and mosaic female *Mecp2*$^{tm1.1Bird/+}$ isocortices (Fig. 5A and B). There were no differences in the maximal respiration induced by uncoupling mitochondria with the protonophore carbonyl cyanide 4-(trifluoromethoxy)phenylhydrazone (FCCP. Figure 5A and C). Differentiated mutant LUHMES cells (Fig. 5D–F) and HAP1 cells (Fig. 5J–L) had decreased basal and maximal mitochondrial respiration parameters. In contrast, a 2-fold increase in both respiration parameters was observed in *MECP2* mutant SH-SY5Y cells (Fig. 5G–I). The same oxygen consumption phenotypes were observed when respiration was monitored continuously for 48 h with Resipher platinum sensing probes in HAP1 and SH-SY5Y (Supplementary Fig. S8A and C) [58, 59]. Neither could we observe

period oscillations in respiration in wild type and *MECP2* mutant cells (Supplementary Fig. S8A and C), nor respiration phenotypes be attributed to differences in cell numbers (Supplementary Fig. S8A–C). These results support cell-type dependent mitochondrial respiration phenotypes in *Mecp2/MECP2* mutants.

We previously demonstrated that decreased mitochondrial respiration in mutant LUHMES cells can be restored by reintroduction of the *MECP2* gene [40]. Similar gene re-expression experiments were performed in HAP1 cells. We chose to conduct these experiments in HAP1 cells because respirometry has the lowest sampling variability as assessed by 95% confidence intervals (compare shaded brackets in Fig. 5D, G and J). HAP1 MECP2 knockout cells stably expressing mouse Mecp2-GFP (Fig. 5M, lanes 3–4) or GFP alone as a control were generated (Fig. 5M, lane 6) [60]. The expression of recombinant mouse Mecp2-GFP or GFP was confirmed by immunoprecipitation with GFP antibodies followed by GFP immunoblotting (Fig. 5M compare lanes 2 with 3–4). Expression of Mecp2-GFP in *MECP2*-null cells increased respiration as determined by minimally overlapping 95% confidence intervals (Fig. 5N). Both basal and maximal respiration were increased by expressing Mecp2-GFP in two independent clones as compared to *MECP2*-null cells expressing GFP alone (Fig. 5O and P). The results indicate that mitochondrial respiration is modulated by the expression of Mecp2 in a cell-type dependent manner.

Consumption of exogenously added pyruvate is impaired in *MECP2* mutants

Differentiated LUHMES and HAP1 *MECP2* mutant cells have decreased mitochondrial respiration that can be increased by the expression of the *Mecp2/MECP2* gene. However, these cells do not change their mitochondrial carrier Mpc1 levels (Fig. 4F and H). This observation can be interpreted in two ways: first, defective respiration could be related to Mpc1 function rather than absolute Mpc1 levels in these cells. Alternatively, mutant cells could have compromised mitochondrial pyruvate utilization by mechanisms downstream of Mpc1. To discriminate between these two mechanisms, the ability of *Mecp2/MECP2* mutant cells to use exogenously added pyruvate as the only mitochondrial fuel source was assessed. As a benchmark, *Mpc1* mutant cells preferentially compromise their FCCP-induced maximal respiration when pyruvate is the only fuel source exogenously offered to cells. This defect can be bypassed by offering glutamine as a mitochondrial fuel to Mpc1 mutant cells (Fig. 6A) [61–63].

Mitochondrial respiration was first measured in wild type, $Mecp2^{tm1.1Bird/y}$ and mosaic female $Mecp2^{tm1.1Bird/+}$ isocortical cultures by Seahorse respirometry in media with pyruvate as the only source of fuel. A small but significant decrease in the maximal respiratory capacity in both pyruvate-fed primary neuronal cultures of *Mecp2*-null male and *Mecp2* mosaic female mice was documented (Fig. 6B–D). The small dynamic range of this pyruvate-fed isocortex phenotype prevented further study of fuel preferences by these cells. We therefore assessed HAP1 cells (Fig. 6E–I) as their MECP2 mutant proteome has the biggest overlap with the *Mecp2* mutant mouse brain proteome (Supplementary Fig. S7B). Respiration in intact cells incubated in glucose-, pyruvate- and glutamine-free (fuel-free) media was assessed. Pyruvate or a mix of glucose, pyruvate and glutamine (complete media) were then acutely added as fuel sources (Fig. 6E–I). Compared to wild type cells, *MECP2* mutant cells showed impaired respiration irrespective of the fuel source (Fig. 6E). Addition of pyruvate increased respiration of wild type cells as compared to fuel-free media (Fig. 6F compare columns 1–2). However, this response was half the magnitude observed in wild type cells fed complete media (Fig. 6F compare columns 2–3). In contrast, there was no difference in the magnitude of the increase in respiration rate when *MECP2*-null cells were acutely fed pyruvate-containing or complete media (Fig. 6F compare columns 5–6). Addition of FCCP increased respiration in wild type cells fed pyruvate-only or complete-media (Fig. 6G compare columns 1 with 2–3). However, *MECP2* mutant cells failed to undergo an FCCP-dependent increase in mitochondrial respiration when the only source of fuel was pyruvate (Fig. 6G compare columns 4–5). These mutant cells increased their FCCP-dependent respiration when fed complete media (Fig. 6G compare columns 4–5 with 6). This suggest that fuels other than pyruvate, like glutamine, mediate the increased FCCP-induced maximal respiration observed in mutant cells (Fig. 6A).

We compared basal and maximal respiration in wild type and *MECP2* mutant cells where the only source of fuel was either increasing concentrations of pyruvate or glutamine (Fig. 6H-I). Basal and maximal respiration increased with increasing concentrations of pyruvate in wild type cells. However, *MECP2* mutants failed to increase either respiratory parameter when fed increasing concentrations of pyruvate (Fig. 6H compare circles and triangles). In contrast to cells fed pyruvate, maximal respiration was similar between wild type and mutant cells when the only source of extracellular fuel was glutamine (Fig. 6I compare circles and triangles). These results demonstrate that HAP1 *MECP2* mutant cells have a defect in the utilization of exogenously added pyruvate when mitochondria are uncoupled with FCCP. These findings support the conclusion that mitochondria from *MECP2* mutant cells have a defect utilizing pyruvate that phenocopies Mpc1 gene defects.

Mitochondrial consumption of pyruvate is impaired in *MECP2* mutants

We next assessed whether *MECP2* mutant cells consume glycolysis-generated endogenous pyruvate by measuring respiration after a galactose switch, a condition where glucose is replaced by galactose in media. This switch halts glycolysis, thus the endogenous production of pyruvate from glucose, and renders cell ATP supply dependent solely on mitochondrial respiration (Fig. 7A) [64–66]. Under a galactose switch, cells use glutamine as a major fuel source for respiration (Fig. 7A) [66]. We reasoned that if *MECP2* mutant cells have impaired mitochondrial pyruvate utilization but normal glutamine utilization (Fig. 6H and I), then *MECP2* respiration should be similar to wild type respiration only in galactose-containing media. Seahorse respirometry was performed in wild type and mutant cells in media containing either glucose, pyruvate, and glutamine (complete glucose media) or the same formulation where glucose was replaced by galactose (complete galactose media) as well as controls for both media formulations that excluded glutamine (Fig. 7B–E). Complete galactose media changed the stress test respiration profile in both cell types in a glutamine-sensitive manner (compare dark and light symbols, Fig. 7B and C). The decreased respiration phenotype observed in *MECP2*-null cells was overt in complete glucose media, but wild type and mutant respiration became indistinguishable in complete galactose media (Fig. 7B and C).

Wild type basal respiration was comparable in complete glucose and galactose media (Fig. 7D compare columns 1–2). In contrast, *MECP2* mutant cells increased their basal respiration to wild type levels in complete galactose media as compared

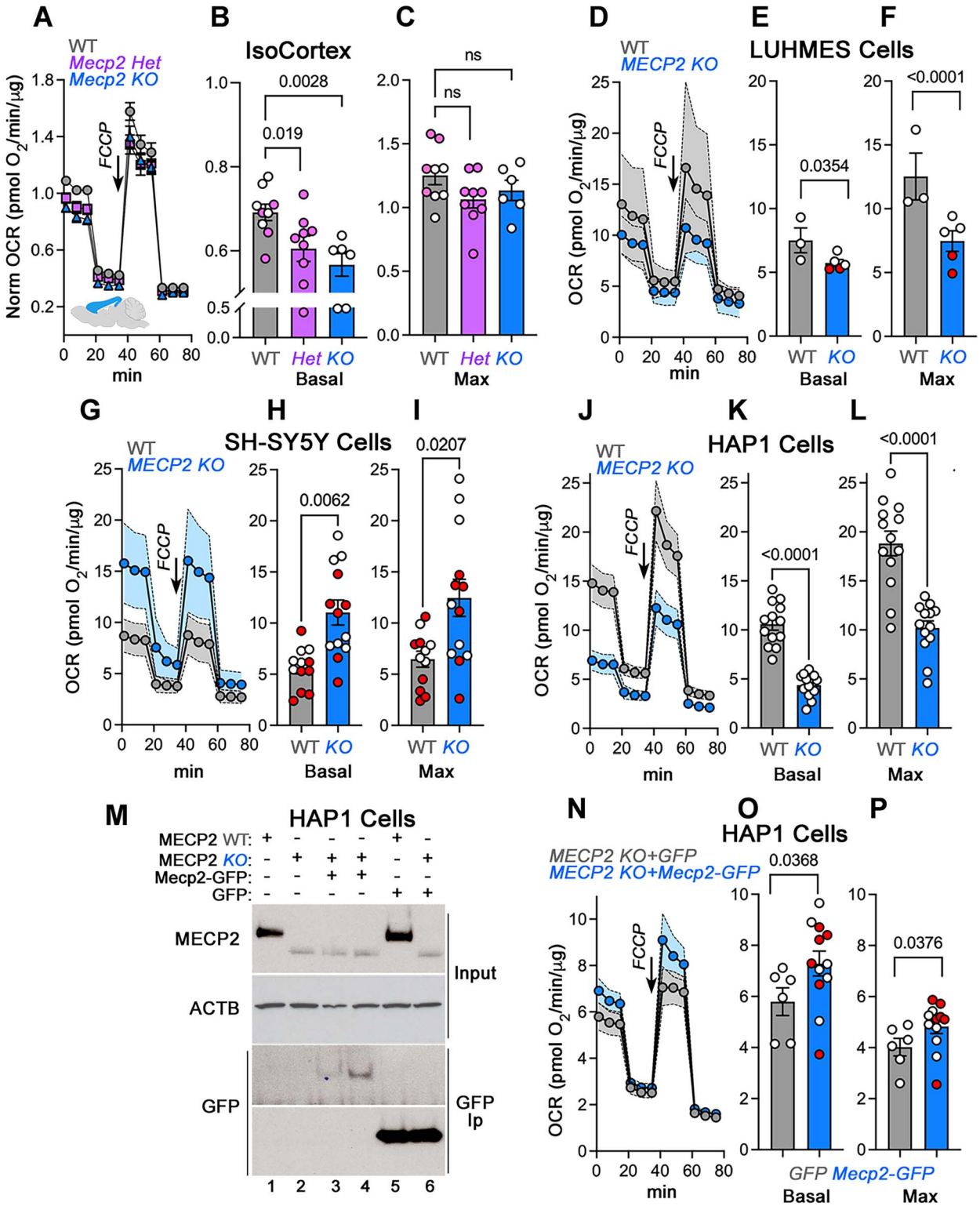

Figure 5. Mitochondrial respiration is altered in *Mecp2*$^{tm1.1Bird/y}$ isocortex primary cultures and *MECP2* mutant cells. (A–C) Primary cultured isocortex neurons from postnatal day 1 cultured for 14 days were subjected to a seahorse stress test in the presence of complete media. Oxygen consumption rate was normalized to wild type animal values at measurement 3. (B) Depicts basal respiration and (C) presents maximal respiration elicited after FCCP addition (arrow). Each symbol corresponds to an independent animal, colored symbols mark female animals. D–F show mitochondrial stress test, basal and maximal respiration in wild type and *MECP2*-null differentiated LUHMES cells. (G–I) Depict mitochondrial stress test, basal, and maximal respiration in wild type and *MECP2*-null differentiated SH-SY5Y neuroblastoma cells. (J–L) mitochondrial stress test, basal, and maximal respiration in wild type and *MECP2*-null HAP1 cells. (M) Wild type (lane 1), stably expressing GFP (lane 5) and MECP2-null HAP1 cells (lane 2), stably expressing GFP (lane 6) or mouse *Mecp2*-GFP (lanes 3-4) were immunoprecipitated with anti-GFP antibodies and analyzed by immunoblot with antibodies against GFP. (N–P) Depict mitochondrial stress test, basal, and maximal respiration in *MECP2*-null HAP1 cells stably expressing GFP (gray symbols) or *Mecp2*-GFP (blue symbols). (D, G, J and N) brackets and shaded area show average ± 95 confidence interval. Inflection after datapoint 3 marks addition of oligomycin and drop after datapoint 9 marks addition of rotenone and antimycin. All other data show average ± SEM. Each symbol is an independent biological replicate. Colored symbols show an independent clone isolate. p Values were obtained with two-sided permutation t-test with 5000 bootstrap samples.

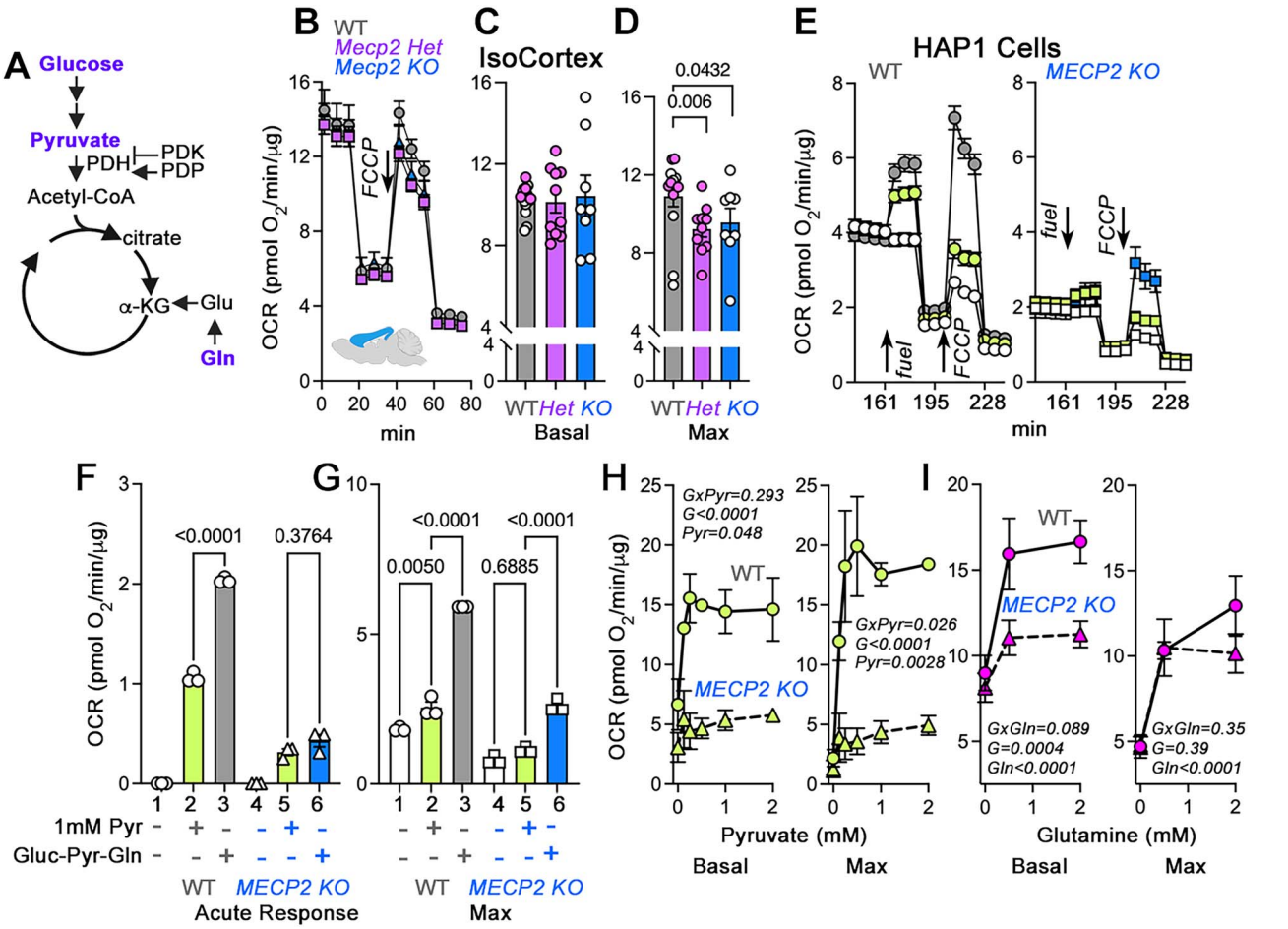

Figure 6. Exogenous pyruvate and glutamine differentially support mitochondrial respiration in *Mecp2*$^{tm1.1Bird/y}$ isocortex primary cultures and *MECP2* mutant cells. (A) Diagram of key glycolysis and Krebs cycle steps analyzed. Purple font indicates metabolites experimentally manipulated. (B–D) Primary cultured isocortex neurons from postnatal day 1 cultured for 14 days were subjected to a Seahorse stress test in the presence of media with 1 mM pyruvate as the only fuel source. (C) Depicts basal respiration and (D) presents maximal respiration elicited after FCCP addition (arrow). Each symbol corresponds to an independent animal, colored symbols mark female animals. p Values were obtained with two-sided permutation t-test with 5000 bootstrap samples. (E–G) Show mitochondrial stress test, acute response to fuel addition, and maximal respiration in wild type and *MECP2*-null HAP1 cells in media without fuel (white symbols) complete media (see F for color codes), or media with 1 mM pyruvate (see F for color codes). For E, inflection after data point 4 marks addition of the fuel source to basal media. One-way ANOVA followed by Bonferroni corrections. Each symbol represents an independent biological replicate. Arrows indicate fuel and FCCP additions. H, I depict mitochondrial basal, and maximal respiration in wild type and *MECP2*-null HAP1 cells fed media in the absence or presence of increasing concentrations of either pyruvate (H) or glutamine (I). For H n = 2 and for I n = 8. Two-way ANOVA where factors are genotype (G) and fuel, followed by Benjamini, Krieger and Yekutieli corrections. (B and E) Inflections after datapoint 3 or 7 respectively, mark addition of oligomycin and drop after datapoint 9 or 13 marks addition of rotenone and antimycin. All data show average ± SEM.

to complete glucose media (Fig. 7D compare columns 2 and 6). Basal respiration was decreased to similar levels in glutamine-free media for both genotypes (Fig. 7D compare columns 1–2 with 3–4, 5–6 with 7–8). The effect of the galactose switch and its glutamine-dependency were also evident when measuring FCCP-induced maximal respiration (Fig. 7E). Wild type maximal respiration decreased by 50% in complete galactose media as compared to glucose complete media, reflecting a requirement of endogenous pyruvate (Fig. 7E compare columns 1–2). In contrast, the FCCP-induced maximal respiration drop by only 30% in complete galactose media but to the same level observed in wild type galactose media-treated cells (Fig. 7E compare columns 2 and 6). These respiratory parameters were similarly dependent on the presence of glutamine in the media in both genotypes (Fig. 7E compare columns 1–2 with 3–4, 5–6 with 7–8). We directly measured the utilization of pyruvate by mitochondrial by measuring the conversion of $^{13}C_3$-pyruvate to ^{13}C-labeled Krebs cycle intermediaries (Fig. 7F). Mutant MECP2 cells showed significantly decreased conversion of labeled pyruvate into Krebs cycle carboxylic acids as compared to wild type (Fig. 7F). We conclude that *MECP2* deficient mitochondria have impaired utilization of endogenous pyruvate as a fuel source while maintaining normal consumption of glutamine for respiration.

We assessed alternative mechanisms that could account for the impaired pyruvate utilization in *MECP2* mutant cells, other than the levels of the pyruvate transporter Mcp1. The pyruvate dehydrogenase complex (PDH, Fig. 7A, G and H) is a key regulatory hub in carbohydrate metabolism that links pyruvate produced by glycolysis to the mitochondrial tricarboxylic acid cycle via its product acetyl-CoA, which is turned into citrate (Fig. 7A and H) [67]. The activity of PDH is inhibited by phosphorylation of its PDHA1 subunit, a process under dynamic control of mitochondrial kinases (PDK, Fig. 7A, G and H) and phosphatases (PDP, Fig. 7A, G and H) [68]. The abundance of PDH complex subunits

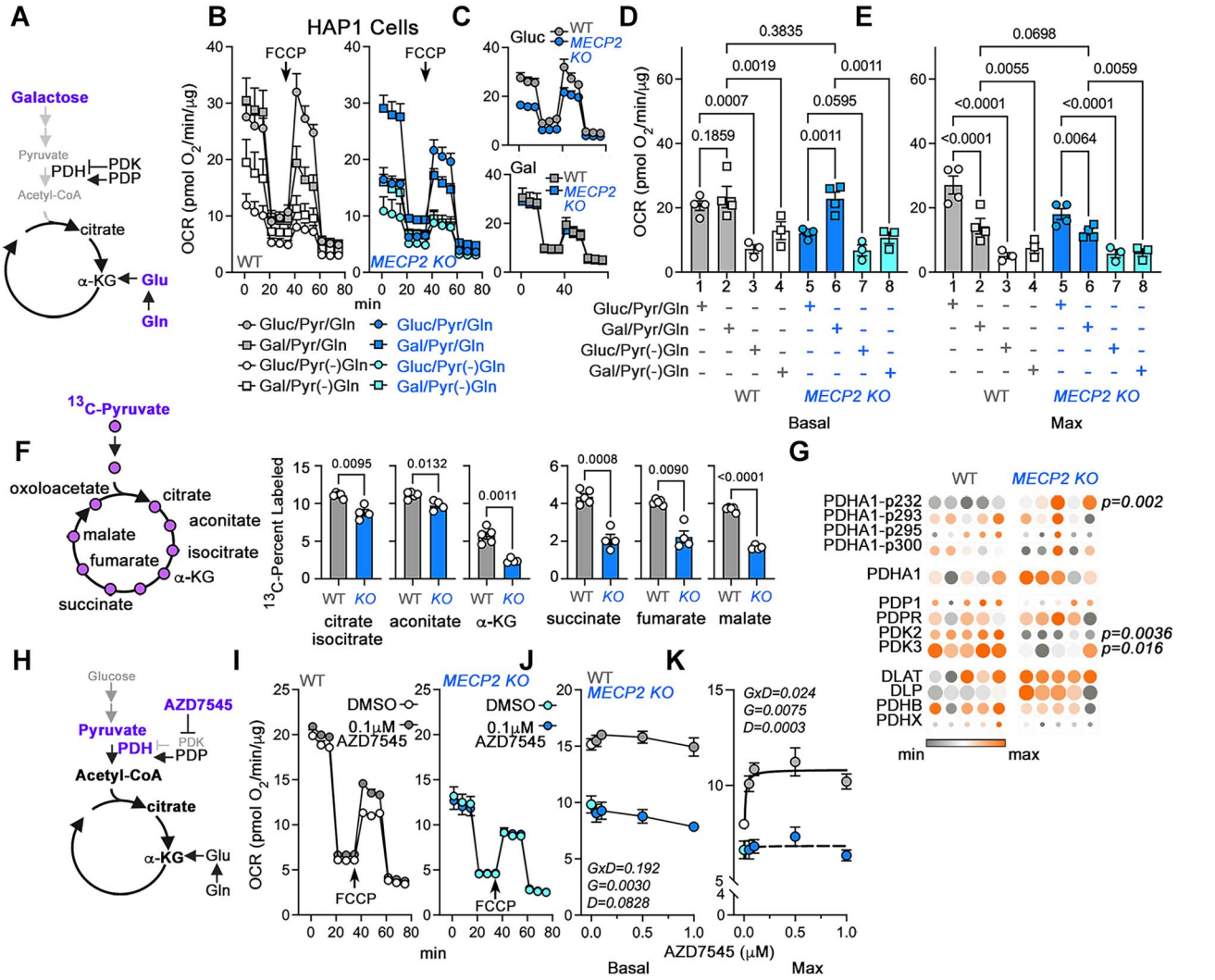

Figure 7. The utilization of endogenous pyruvate for mitochondrial respiration is selectively impaired in *MECP2* mutant cells. (A) Diagram of key glycolysis and Krebs cycle steps analyzed. Purple font indicates metabolites experimentally manipulated. (B–E) Show mitochondrial stress test, basal, and maximal respiration in wild type (white and gray symbols) and *MECP2*-null HAP1 cells (blue and teal symbols) in glucose and galactose complete media with or without glutamine [(−)Gln]. (C) Compares complete glucose and galactose media in wild type and mutant cells shown in B. (D, E) Each symbol represents an independent biological replicate. One-way ANOVA followed by Benjamini, Krieger and Yekutieli corrections. (F) Conversion of $^{13}C_3$-pyruvate into metabolites of the Krebs cycle in wild type and *MECP2*-null HAP1 cells (blue bars), n = 5. (G) Heat map of the proteome and phosphoproteome $\log_2$ normalized expression levels for subunits of the pyruvate dehydrogenase complex, pyruvate dehydrogenase kinases and subunits of the pyruvate dehydrogenase phosphatase in wild type and *MECP2*-null HAP1 cells. Each column is an independent biological replicate. For F and G, p values were obtained with two-sided permutation t-test with 5000 bootstrap samples. (H) Diagram of key glycolysis and Krebs cycle steps analyzed. Purple font indicates metabolites experimentally manipulated or drugs added and their target. (I) Mitochondrial stress test, (J), basal, and (K), maximal respiration in wild type and *MECP2*-null HAP1 cells fed 1 mM pyruvate media in the presence of vehicle or increasing concentrations of AZD7545. (I–K) n = 4. (I and J) Mixed-effect analysis where factors are genotype (G) and drug (D), followed by Šídák's multiple comparisons test. (B, C and I) Inflections after datapoint 3 marks addition of oligomycin and drop after datapoint 9 marks addition of rotenone and antimycin. All data show average ± SEM.

was quantified by mass spectrometry (CORUM complex ID 1375; PDH1, DLAT, DLP, PDHB, and PDHX) [69], PDH1 phosphopeptides, PDH kinases (PDK2 and 3), and the PDH phosphatase catalytic and regulatory subunits (PDP1 and PDPR, Fig. 7G) [67]. A significant increase in the phosphorylation of PDHA1 at position 232 was identified without changes in the total abundance of PDHA1 or other subunits of the PDH complex (Fig. 7G). PDHA1 phosphorylation at position 232 inhibits PDH enzymatic activity [70, 71]. The increased PDHA1 phosphorylation could not be explained either by elevated steady-state levels of kinases or by decreased phosphatase levels (Fig. 7G). These findings suggest that changes in the enzymatic activity of either the kinase or the phosphatase in *MECP2*-null cells as a potential mechanism for PDHA1 phosphorylation at position 232. To discriminate between an increased kinase activity or a decreased phosphatase activity regulating PDHA1 phosphorylation, the effect of the PDK inhibitor AZD7545 [72] was assessed by Seahorse respirometry with pyruvate as the only fuel source (Fig. 7H–K). AZD7545 increased FCCP-induced maximal respiration in wild type cells, suggesting that a steady-state kinase activity acts as a brake in the utilization of pyruvate (Fig. 7I and K). In contrast, AZD7545 did not modify the FCCP-induced maximal respiration in *MECP2* mutant, a finding consistent with a model where an already decreased phosphatase activity hinders the utilization of pyruvate by the mitochondria in *MECP2*-deficient cells (Fig. 7J and K). We conclude that the *MECP2* gene defect impairs pyruvate mitochondrial

utilization through a post-translational mechanism that inhibits the PDH complex.

Discussion

To date, Rett syndrome research has primarily focused on neuronal mechanisms of disease with an emphasis on transcriptome studies. However, MECP2 is expressed in most organs with protein levels similar to those in the brain [4]. This finding suggests that mutations in this gene have systemic effects that contribute to disease burden [5–7]. We comprehensively assessed steady-state levels of transcripts and proteins in multiple organs and brain regions from *Mecp2*-null mice to determine the extent to which mutations in this gene impact the whole organism. Our findings reveal that the transcriptomes and proteomes of cortex, liver, kidney and skeletal muscle undergo extensive modifications in *Mecp2*$^{tm1.1Bird/y}$ animals that occur before the appearance of overt phenotypes and the onset of mortality. Transcriptome and proteome modifications are most pronounced in brain cortex, liver, kidney and skeletal muscle as compared to hippocampus and striatum, whose transcriptomes and proteomes are modestly affected in *Mecp2* mutants. *Mecp2*-sensitive transcriptomes, but more prominently proteomes, are enriched in metabolic annotated gene products across tissues [5]. The metabolic annotated genes preponderantly represent lipid metabolism and mitochondrial pathways. Importantly, the proteome of the most affected brain region, the *Mecp2* mutant cortex, is enriched for both synaptic and mitochondrial annotated proteins by two-fold, suggesting the potential for comparable contribution of synaptic and mitochondrial processes to the genesis of Rett syndrome brain phenotypes. These findings are in agreement with recent findings in iPSC-derived human MECP2 mutant astrocytes [73, 74]. We conclude that mutations in *Mecp2* cause a systemic disorder affecting lipid and mitochondrial metabolism.

Our lipid and mitochondrial metabolic findings suggest a dysregulation of pyruvate-acetyl-CoA metabolism in *Mecp2*/*MECP2* tissues and cells. Acetyl-CoA synthesis is tied to the entry and metabolization of pyruvate by mitochondria, which we show is perturbed in *MECP2* mutant cells [75]. Among the mutant tissues whose proteomes revealed altered metabolic pathways, the *Mecp2*-mutant liver proteome stands-out. We note that 10 of the 17 enzymes in the cholesterol synthesis pathway have decreased steady-state protein levels in *Mecp2* mutant liver. The robustness of this finding is supported by replication in an independent cohort of animals (data not shown). The cholesterol synthesis pathway begins with acetyl-CoA as a primary substrate. Among these 10 cholesterol synthesis enzymes down-regulated in the *Mecp2* liver, we note that squalene epoxidase (*Sqle*) encodes a rate-limiting enzymes in the cholesterol synthesis pathway [76]. Importantly, single copy mutation of the *Sqle* gene rescues *Mecp2*-null phenotypes revealing the centrality of this metabolic pathway to a *Mecp2*-null mouse model and the capacity of our proteome studies to capture this important disease biology [15, 16]. Other lipid metabolism proteins that generate acetyl-CoA are increased in *Mecp2* mutant liver. Acss3, a mitochondrial propionate-CoA ligase, catalyzes the synthesis of acetyl-CoA from short fatty acids [77]. Increased expression of Acss3 may be adaptive and normalize availability of acetyl-CoA. This concept is supported by a genetic suppressor screen demonstrating that mutations in acetoacetate-CoA ligase (*Aacs*) suppress phenotypes in *Mecp2*$^{tm1.1Bird/y}$ mice [15]. *Aacs* encodes a acetoacetyl-CoA synthetase that takes acetyl-CoA to funnel it to the cholesterol synthesis pathway [78]. The hypothesis that a pyruvate-acetyl-CoA axis is regulated by the Mecp2 protein is supported by the results in cerebrospinal fluid from *Mecp2*-null mouse documenting changes in the levels of mitochondrial factors that metabolize pyruvate [40]. *Mecp2* deficiency has also been reported to decrease levels of pyruvate dehydrogenase E1 subunit beta, and levels of this subunit are restored when *Mecp2* is re-expressed [79]. Additional evidence for a dysregulated pyruvate-acetyl-CoA axis is the observation that pyruvate increases in cortex of *Mecp2*$^{tm1.1Bird/y}$ mice [80]. Elevated pyruvate levels have also been documented in the CSF of Rett patients [81–83] and in plasma [10]. Similarly, human astrocytes carrying mutations in *MECP2* have decreased levels of intracellular citrate [73, 74]. These consistent findings support the idea that impaired utilization of pyruvate is a common Rett syndrome phenotype.

Our findings in *Mecp2* mutant liver cholesterol pathways differ from those previously reported. However, there are differences in study designs that may explain this apparent discrepancy [14–16]. First, we analyzed animals at 45 days rather than 56 days. This age difference is important as *Mecp2*$^{tm1.1Bird/y}$ mice aged to 56 days experience a mortality rate near 50% and most mutants experience neurological symptoms [32]. Second, we studied *Mecp2* mutant livers that were devoid of overt fatty liver pathology. This suggest that liver pathology in Rett syndrome models evolves with age and may be initiated by a mechanism that indirectly involves transcriptional control by Mecp2 before the onset of fatty liver [14].

Our results expand the evidence indicating that Rett syndrome is a systemic metabolic disease that affects neurodevelopment [5]. Considering the Rett syndrome, and other disorders of neurodevelopment, as systemic diseases provides the conceptual basis to expand biomarker and therapeutic discovery [84]. Specifically, other more accessible tissues have potential to serve as a proxy for brain disease mechanisms and therapies. For example, *Mecp2* defective cholesterol synthesis pathways in liver have a parallel in brain where de novo synthesis of cholesterol is diminished [16]. Brain and liver defects in cholesterol synthesis may be linked to changes in the content of HDL lipoproteins in the cerebrospinal fluid of *Mecp2* mutant animal and neuronal models as well as in *Mecp2*$^{tm1.1Bird/y}$ mouse plasma (unpublished results) [40]. These findings suggest that a plasma biomarker assessing a Rett syndrome liver phenotype has potential to correlate with similar processes in brain. Similarly, therapeutics that ameliorate peripheral tissue phenotypes could act as a proxy for the effectiveness of those therapies in brain. Take for example the therapeutic use of short fatty acid-rich or ketogenic diets that bypass the need of pyruvate as a mitochondrial fuel in Rett syndrome. These nutrients can improve *Mecp2* mouse mutant behaviors, survival, and modify liver and muscle metabolic phenotypes [85]. Similarly, ketogenic dietary interventions have been reported to improve neurological and behavioral phenotypes in Rett patient case reports. The effectiveness of this treatment may be more widespread and awaits results from ongoing clinicaltrials [86, 87].

There are two findings that support novel mechanisms of disease. First is the variable correlation of *Mecp2*-null transcriptomes and proteomes within a tissue. The second is a selective metabolic defect in the utilization of pyruvate by *MECP2*-mutant cells yet normal utilization of glutamine as a carbon source for respiration. *Mecp2*-sensitive mRNAs and protein steady-state levels strongly correlate in liver. In contrast, changes in the transcriptome of the *Mecp2* mutant cortex do not correlate with the changes in the proteome. The simplest explanation for this lack of correlation in cortex would be technical problems with either the proteome or transcriptome assays or data processing pipelines. However,

this is unlikely for several reasons. First, we performed all tissue analyses simultaneously, therefore technical problems with brain tissue should have also affected analyses performed in the other tissues. Second, we validated our transcriptome against multiple replication benchmarks. Third, we asked how well the wild type cortex transcriptome and proteome correlate to find that the Spearman correlation is 0.38. This value is within the range of similar correlations across tissues, including nervous tissue, and diverse cells (Spearman 0.24–0.65) [88–92]. Finally, our proteomics shows strong ontological/pathway convergence with a previous *Mecp2* mutant mouse brain cortex proteome [43]. Confidence in the validity of our analyses is further increased by the robustness of the replication despite considerable differences in methodology including a different *Mecp2* animal model, timing and method of tissue collection, the mass spectrometry strategy, and data processing between our study and those employed for the whole isocortex proteome [43]. Furthermore, the ontological/pathway similarity of the mouse brain *Mecp2* cortex proteome extends to the mouse and rat cerebrospinal *Mecp2* mutant proteomes demonstrating robustness in pathway identification in *Mecp2* mutant brain [40]. Our data suggest that the poor correlation between the *Mecp2*-sensitive brain transcriptomes and proteomes may be disease phenotype. Divergency between the *Mecp2*-sensitive brain transcript and protein levels could be explained by posttranscriptional or posttranslational mechanisms. A factor contributing to transcriptome-proteome divergence is a spatial segregation of the transcriptome from the proteome that it controls, such as dissimilar localization of the transcript and the protein it encodes at an anatomical/subcellular level [93, 94]. Transcriptomes could also be more susceptible to cell diversity than the proteome. Brain and liver have marked differences in cell type diversity but cellular type diversity is similar between skeletal muscle and liver [95]. Nonetheless, muscle and liver have pronounced differences in the correlation of their transcriptome-proteome correlations. Finally, we explored whether small regulatory RNAs under the control of *Mecp2* could account for modifying transcriptome output [96]. We measured the levels of microRNAs in microdissected cortex and liver were quantified as these two tissues had the most pronounced differences in their transcriptome-proteome correlations. The predicted targets of the microRNAs that have altered expression with *Mecp2* mutations only minimally overlap with cortex and liver transcript and proteins affected by the *Mecp2* mutation. These findings do not support the hypothesis that MECP2 protein indirectly regulates translation through regulation of microRNAs. It is likely that other tissue-specific regulatory factors or combinations of thereof explain *Mecp2*-mutant transcriptome-proteome divergency. Potential mechanisms include differences in RNA stability, a proteome with a delayed response to modifications of the transcriptome, as well as changes in the rate of protein synthesis and/or degradation [93, 94]. Some of the mechanisms may be intertwined, as recently demonstrated in *MECP2*-mutant iPSC-derived neurons where a global decrease of the active translatome and a decrease in mTOR-dependent protein synthesis impact proteins levels, including components of the protein degradation machinery [97]. Since the translatome varies across development and tissues, and is modified by the metabolic status, it is reasonable to speculate that the differences observed across *Mepc2*/*MECP2* mutant tissue transcriptome-proteome correlations are determined, in part, by cell-autonomous translational, post-translational, and metabolic landscapes [96–101].

Another novel finding is the *MECP2*-mutant defect in pyruvate utilization yet normal consumption of glutamine for respiration. We think this observation reveals an impaired metabolic flexibility phenotype, a hallmark of metabolic diseases. Mitochondria modify the quality and quantity of the carbon substrate oxidized by mitochondria, a process known as metabolic flexibility [102, 103]. The plasticity in the quality and/or magnitude of mitochondrial substrates utilized is determined by the tissue functional demand, organism metabolic status (lean or obese), developmental stage, the availability of nutrients, or a pathological condition such as diabetes [102, 103]. The fetal brain relies on aerobic glycolysis but at birth it progressively transitions to consumption of oxygen and glucose reaching a maximum around postnatal age five years [104–107]. Pyruvate derived from glycolysis is a key metabolite whose entry to mitochondria, modulates carbon utilization preferences between glucose, aminoacids, ketones, and lipids [108, 109]. In the case of neurons, pyruvate-dependent metabolic flexibility couples the activity of the synapse to the production of ATP by synaptic mitochondria [110, 111]. The changes in expression of either the pyruvate carrier Mpc1 or the NAD^+ carrier Slc25a51 in *Mecp2* mutant brains support the idea of defective metabolic flexibility in neural tissue. Thus, impaired metabolic flexibility could contribute to synaptic phenotypes in Rett syndrome and other neurodevelopmental disorders [112].

Supplementary data

Supplementary data is available at *HMG Journal* online.

Funding

V.F. was funded by the Rett Syndrome Research Trust, the Loulou Foundation, and by National Institutes of Health NIH 1RF1AG060285. K.S.S. holds a Postdoctoral Enrichment Program Award from the Burroughs Wellcome Fund and is supported by National Institutes of Health NIH K00NS108539.

Conflict of interest statement: None declared.

Data availability

All data are available upon request.

References

1. Amir RE, Van den Veyver IB, Wan M. *et al.* Rett syndrome is caused by mutations in X-linked MECP2, encoding methyl-CpG-binding protein 2. *Nat Genet* 1999;**23**:185–8.
2. Sandweiss AJ, Brandt VL, Zoghbi HY. Advances in understanding of Rett syndrome and MECP2 duplication syndrome: prospects for future therapies. *Lancet Neurol* 2020;**19**:689–98.
3. Chahrour M, Zoghbi HY. The story of Rett syndrome: from clinic to neurobiology. *Neuron* 2007;**56**:422–37.
4. Schmidt T, Samaras P, Frejno M. *et al.* ProteomicsDB. *Nucleic Acids Res* 2018;**46**:D1271–81.
5. Kyle SM, Vashi N, Justice MJ. Rett syndrome: a neurological disorder with metabolic components. *Open Biol* 2018;**8**:170216.
6. Vashi N, Justice MJ. Treating Rett syndrome: from mouse models to human therapies. *Mamm Genome* 2019;**30**:90–110.
7. Borloz E, Villard L, Roux JC. Rett syndrome: think outside the (skull) box. *Fac Rev* 2021;**10**:59.
8. Philippart M, Opitz JM, Reynolds JF. Clinical recognition of Rett syndrome. *Am J Med Genet Suppl* 1986;**1**:111–8.
9. Jellinger K, Armstrong D, Zoghbi HY. *et al.* Neuropathology of Rett syndrome. *Acta Neuropathol* 1988;**76**:142–58.

10. Neul JL, Skinner SA, Annese F. *et al.* Metabolic signatures differentiate Rett syndrome from unaffected siblings. *Front Integr Neurosci* 2020;**14**:7.
11. Kohda M, Tokuzawa Y, Kishita Y. *et al.* A comprehensive genomic analysis reveals the genetic landscape of mitochondrial respiratory chain complex deficiencies. *PLoS Genet* 2016;**12**:e1005679.
12. Liu C, Wang J, Wei Y. *et al.* Fat-specific knockout of Mecp2 upregulates Slpi to reduce obesity by enhancing browning. *Diabetes* 2020;**69**:35–47.
13. Vashi N, Ackerley C, Post M. *et al.* Aberrant lung lipids cause respiratory impairment in a Mecp2-deficient mouse model of Rett syndrome. *Hum Mol Genet* 2021;**30**:2161–76.
14. Kyle SM, Saha PK, Brown HM. *et al.* MeCP2 co-ordinates liver lipid metabolism with the NCoR1/HDAC3 corepressor complex. *Hum Mol Genet* 2016;**25**:3029–41.
15. Enikanolaiye A, Ruston J, Zeng R. *et al.* Suppressor mutations in Mecp2-null mice implicate the DNA damage response in Rett syndrome pathology. *Genome Res* 2020;**30**:540–52.
16. Buchovecky CM, Turley SD, Brown HM. *et al.* A suppressor screen in Mecp2 mutant mice implicates cholesterol metabolism in Rett syndrome. *Nat Genet* 2013;**45**:1013–20.
17. Barr JB, Somerville RA, Chung YL. *et al.* Microdissection: a method developed to investigate mechanisms involved in transmissible spongiform encephalopathy pathogenesis. *BMC Infect Dis* 2004;**4**:8.
18. Shah RR, Cholewa-Waclaw J, Davies FCJ. *et al.* Efficient and versatile CRISPR engineering of human neurons in culture to model neurological disorders. *Wellcome Open Res* 2016;**1**:13.
19. Andrews S. FastQC: A Quality Control Tool for High Throughput Sequence Data 2010. http://www.bioinformatics.babraham.ac.uk/projects/fastqc/.
20. Afgan E, Baker D, Batut B. *et al.* The Galaxy platform for accessible, reproducible and collaborative biomedical analyses: 2018 update. *Nucleic Acids Res* 2018;**46**:W537–44.
21. Kim D, Langmead B, Salzberg SL. HISAT: a fast spliced aligner with low memory requirements. *Nat Methods* 2015;**12**:357–60.
22. Liao Y, Smyth GK, Shi W. featureCounts: an efficient general purpose program for assigning sequence reads to genomic features. *Bioinformatics* 2014;**30**:923–30.
23. Love MI, Huber W, Anders S. Moderated estimation of fold change and dispersion for RNA-seq data with DESeq2. *Genome Biol* 2014;**15**:550.
24. Biedler JL, Roffler-Tarlov S, Schachner M. *et al.* Multiple neurotransmitter synthesis by human neuroblastoma cell lines and clones. *Cancer Res* 1978;**38**:3751–7.
25. Ping L, Kundinger SR, Duong DM. *et al.* Global quantitative analysis of the human brain proteome and phosphoproteome in Alzheimer's disease. *Sci Data* 2020;**7**:315.
26. Higginbotham L, Ping L, Dammer EB. *et al.* Integrated proteomics reveals brain-based cerebrospinal fluid biomarkers in asymptomatic and symptomatic Alzheimer's disease. *Sci Adv* 2020;**6**:eaaz9360.
27. Bindea G, Mlecnik B, Hackl H. *et al.* ClueGO: a Cytoscape plug-in to decipher functionally grouped gene ontology and pathway annotation networks. *Bioinformatics* 2009;**25**:1091–3.
28. Shannon P, Markiel A, Ozier O. *et al.* Cytoscape: a software environment for integrated models of biomolecular interaction networks. *Genome Res* 2003;**13**:2498–504.
29. Zhou Y, Zhou B, Pache L. *et al.* Metascape provides a biologist-oriented resource for the analysis of systems-level datasets. *Nat Commun* 2019;**10**:1523.
30. Licursi V, Conte F, Fiscon G. *et al.* MIENTURNET: an interactive web tool for microRNA-target enrichment and network-based analysis. *BMC Bioinformatics* 2019;**20**:545.
31. Ho J, Tumkaya T, Aryal S. *et al.* Moving beyond P values: data analysis with estimation graphics. *Nat Methods* 2019;**16**:565–6.
32. Guy J, Hendrich B, Holmes M. *et al.* A mouse Mecp2-null mutation causes neurological symptoms that mimic Rett syndrome. *Nat Genet* 2001;**27**:322–6.
33. Clemens AW, Wu DY, Moore JR. *et al.* MeCP2 represses enhancers through chromosome topology-associated DNA methylation. *Mol Cell* 2020;**77**:279–293.e8.
34. Wynne ME, Lane AR, Singleton KS. *et al.* Heterogeneous expression of nuclear encoded mitochondrial genes distinguishes inhibitory and excitatory neurons. *eNeuro* 2021;**8**:ENEURO.0232–21.2021.
35. Subramanian A, Tamayo P, Mootha VK. *et al.* Gene set enrichment analysis: a knowledge-based approach for interpreting genome-wide expression profiles. *Proc Natl Acad Sci U S A* 2005;**102**:15545–50.
36. Thompson A, Schafer J, Kuhn K. *et al.* Tandem mass tags: a novel quantification strategy for comparative analysis of complex protein mixtures by MS/MS. *Anal Chem* 2003;**75**:1895–904.
37. Luongo TS, Eller JM, Lu MJ. *et al.* SLC25A51 is a mammalian mitochondrial NAD(+) transporter. *Nature* 2020;**588**:174–9.
38. Moutaoufik MT, Malty R, Amin S. *et al.* Rewiring of the human mitochondrial interactome during neuronal reprogramming reveals regulators of the respirasome and neurogenesis. *iScience* 2019;**19**:1114–32.
39. Rensvold JW, Shishkova E, Sverchkov Y. *et al.* Defining mitochondrial protein functions through deep multiomic profiling. *Nature* 2022;**606**:382–8.
40. Zlatic SA, Duong D, Gadalla KKE. *et al.* Convergent cerebrospinal fluid proteomes and metabolic ontologies in humans and animal models of Rett syndrome. *iScience* 2022;**25**:104966.
41. Koopmans F, van Nierop P, Andres-Alonso M. *et al.* SynGO: an evidence-based, expert-curated knowledge base for the synapse. *Neuron* 2019;**103**:217–234.e4.
42. Rath S, Sharma R, Gupta R. *et al.* MitoCarta3.0: an updated mitochondrial proteome now with sub-organelle localization and pathway annotations. *Nucleic Acids Res* 2021;**49**:D1541–7.
43. Pacheco NL, Heaven MR, Holt LM. *et al.* RNA sequencing and proteomics approaches reveal novel deficits in the cortex of Mecp2-deficient mice, a model for Rett syndrome. *Mol Autism* 2017;**8**:56.
44. Kotecki M, Reddy PS, Cochran BH. Isolation and characterization of a near-haploid human cell line. *Exp Cell Res* 1999;**252**:273–80.
45. Scholz D, Poltl D, Genewsky A. *et al.* Rapid, complete and large-scale generation of post-mitotic neurons from the human LUHMES cell line. *J Neurochem* 2011;**119**:957–71.
46. Samaras P, Schmidt T, Frejno M. *et al.* ProteomicsDB: a multi-omics and multi-organism resource for life science research. *Nucleic Acids Res* 2020;**48**:D1153–63.
47. Pecorelli A, Leoni G, Cervellati F. *et al.* Genes related to mitochondrial functions, protein degradation, and chromatin folding are differentially expressed in lymphomonocytes of Rett syndrome patients. *Mediat Inflamm* 2013;**2013**:137629.
48. Wilhelm BG, Mandad S, Truckenbrodt S. *et al.* Composition of isolated synaptic boutons reveals the amounts of vesicle trafficking proteins. *Science* 2014;**344**:1023–8.
49. Cheng XT, Huang N, Sheng ZH. Programming axonal mitochondrial maintenance and bioenergetics in neurodegeneration and regeneration. *Neuron* 2022;**110**:1899–923.

50. Rangaraju V, Calloway N, Ryan TA. Activity-driven local ATP synthesis is required for synaptic function. *Cell* 2014;**156**: 825–35.
51. Chandel NS. *Lipid Metabolism*, Vol. **13**. Cold Spring Harb Perspect Biol, 2021.
52. Martinez-Reyes I, Chandel NS. Mitochondrial TCA cycle metabolites control physiology and disease. *Nat Commun* 2020;**11**:102.
53. Amici DR, Jackson JM, Truica MI. *et al.* FIREWORKS: a bottom-up approach to integrative coessentiality network analysis. *Life Sci Alliance* 2021;**4**:e202000882.
54. Bowman CE, Zhao L, Hartung T. *et al.* Requirement for the mitochondrial pyruvate carrier in mammalian development revealed by a hypomorphic allelic series. *Mol Cell Biol* 2016;**36**:2089–104.
55. De La Rossa A, Laporte MH, Astori S. *et al.* Paradoxical neuronal hyperexcitability in a mouse model of mitochondrial pyruvate import deficiency. *Elife* 2022;**11**:e72595.
56. Grenell A, Wang Y, Yam M. *et al.* Loss of MPC1 reprograms retinal metabolism to impair visual function. *Proc Natl Acad Sci U S A* 2019;**116**:3530–5.
57. Divakaruni AS, Paradyse A, Ferrick DA. *et al.* Analysis and interpretation of microplate-based oxygen consumption and pH data. *Methods Enzymol* 2014;**547**:309–54.
58. Wit N, Gogola E, West JA. *et al.* A histone deacetylase 3 and mitochondrial complex I axis regulates toxic formaldehyde production. *Sci Adv* 2023;**9**:eadg2235.
59. Grist SM, Chrostowski L, Cheung KC. Optical oxygen sensors for applications in microfluidic cell culture. *Sensors (Basel)* 2010;**10**:9286–316.
60. Tillotson R, Selfridge J, Koerner MV. *et al.* Radically truncated MeCP2 rescues Rett syndrome-like neurological defects. *Nature* 2017;**550**:398–401.
61. Bricker DK, Taylor EB, Schell JC. *et al.* A mitochondrial pyruvate carrier required for pyruvate uptake in yeast, Drosophila, and humans. *Science* 2012;**337**:96–100.
62. Yang C, Ko B, Hensley CT. *et al.* Glutamine oxidation maintains the TCA cycle and cell survival during impaired mitochondrial pyruvate transport. *Mol Cell* 2014;**56**:414–24.
63. Zhang Y, Taufalele PV, Cochran JD. *et al.* Mitochondrial pyruvate carriers are required for myocardial stress adaptation. *Nat Metab* 2020;**2**:1248–64.
64. Arroyo JD, Jourdain AA, Calvo SE. *et al.* A genome-wide CRISPR death screen identifies genes essential for oxidative phosphorylation. *Cell Metab* 2016;**24**:875–85.
65. Marroquin LD, Hynes J, Dykens JA. *et al.* Circumventing the Crabtree effect: replacing media glucose with galactose increases susceptibility of HepG2 cells to mitochondrial toxicants. *Toxicol Sci* 2007;**97**:539–47.
66. Balsa E, Soustek MS, Thomas A. *et al.* ER and nutrient stress promote assembly of respiratory chain supercomplexes through the PERK-eIF2alpha axis. *Mol Cell* 2019;**74**:877–890 e876.
67. Gray LR, Tompkins SC, Taylor EB. Regulation of pyruvate metabolism and human disease. *Cell Mol Life Sci* 2014;**71**: 2577–604.
68. Patel MS, Nemeria NS, Furey W. *et al.* The pyruvate dehydrogenase complexes: structure-based function and regulation. *J Biol Chem* 2014;**289**:16615–23.
69. Hiromasa Y, Fujisawa T, Aso Y. *et al.* Organization of the cores of the mammalian pyruvate dehydrogenase complex formed by E2 and E2 plus the E3-binding protein and their capacities to bind the E1 and E3 components. *J Biol Chem* 2004;**279**: 6921–33.
70. Korotchkina LG, Patel MS. Site specificity of four pyruvate dehydrogenase kinase isoenzymes toward the three phosphorylation sites of human pyruvate dehydrogenase. *J Biol Chem* 2001;**276**:37223–9.
71. Rardin MJ, Wiley SE, Naviaux RK. *et al.* Monitoring phosphorylation of the pyruvate dehydrogenase complex. *Anal Biochem* 2009;**389**:157–64.
72. Kato M, Li J, Chuang JL. *et al.* Distinct structural mechanisms for inhibition of pyruvate dehydrogenase kinase isoforms by AZD7545, dichloroacetate, and radicicol. *Structure* 2007;**15**:992–1004.
73. Sun J, Osenberg S, Irwin A. *et al.* Mutations in the transcriptional regulator MeCP2 severely impact key cellular and molecular signatures of human astrocytes during maturation. *Cell Rep* 2023;**42**:111942.
74. Tomasello DL, Barrasa MI, Mankus D. *et al.* Rett syndrome astrocytes disrupt neuronal activity and cerebral organoid development through transfer of dysfunctional mitochondria. *bioRxiv* 2023, in press. https://doi.org/10.1101/2023.03.02.530903.
75. Guertin DA, Wellen KE. Acetyl-CoA metabolism in cancer. *Nat Rev Cancer* 2023;**23**:156–72.
76. Miller WL, Auchus RJ. The molecular biology, biochemistry, and physiology of human steroidogenesis and its disorders. *Endocr Rev* 2011;**32**:81–151.
77. Yoshimura Y, Araki A, Maruta H. *et al.* Molecular cloning of rat acss3 and characterization of mammalian propionyl-CoA synthetase in the liver mitochondrial matrix. *J Biochem* 2017;**161**:279–89.
78. Ohgami M, Takahashi N, Yamasaki M. *et al.* Expression of acetoacetyl-CoA synthetase, a novel cytosolic ketone body-utilizing enzyme, in human brain. *Biochem Pharmacol* 2003;**65**:989–94.
79. Cortelazzo A, De Felice C, Guy J. *et al.* Brain protein changes in Mecp2 mouse mutant models: effects on disease progression of Mecp2 brain specific gene reactivation. *J Proteome* 2020;**210**:103537.
80. Golubiani G, Lagani V, Solomonia R. *et al.* Metabolomic fingerprint of Mecp2-deficient mouse cortex: evidence for a pronounced multi-facetted metabolic component in Rett syndrome. *Cell* 2021;**10**:2494.
81. Matsuishi T, Urabe F, Komori H. *et al.* The Rett syndrome and CSF lactic acid patterns. *Brain and Development* 1992;**14**: 68–70.
82. Matsuishi T, Urabe F, Percy AK. *et al.* Abnormal carbohydrate metabolism in cerebrospinal fluid in Rett syndrome. *J Child Neurol* 1994;**9**:26–30.
83. Budden SS, Myer EC, Butler IJ. Cerebrospinal fluid studies in the Rett syndrome: biogenic amines and beta-endorphins. *Brain and Development* 1990;**12**:81–4.
84. Faundez V, Wynne M, Crocker A. *et al.* Molecular systems biology of neurodevelopmental disorders, Rett syndrome as an archetype. *Front Integr Neurosci* 2019;**13**:30.
85. Park MJ, Aja S, Li Q. *et al.* Anaplerotic triheptanoin diet enhances mitochondrial substrate use to remodel the metabolome and improve lifespan, motor function, and sociability in MeCP2-null mice. *PLoS One* 2014;**9**:e109527.
86. Haas RH, Rice MA, Trauner DA. *et al.* Therapeutic effects of a ketogenic diet in Rett syndrome. *Am J Med Genet Suppl* 1986;**1**:225–46.
87. Liebhaber GM, Riemann E, Baumeister FA. Ketogenic diet in Rett syndrome. *J Child Neurol* 2003;**18**:74–5.
88. Jiang L, Wang M, Lin S. *et al.* A quantitative proteome map of the human body. *Cell* 2020;**183**:269–283.e19.

89. Wang D, Eraslan B, Wieland T. *et al.* A deep proteome and transcriptome abundance atlas of 29 healthy human tissues. *Mol Syst Biol* 2019;**15**:e8503.
90. Mohammed Y, Bhowmick P, Michaud SA. *et al.* Mouse quantitative proteomics knowledgebase: reference protein concentration ranges in 20 mouse tissues using 5000 quantitative proteomics assays. *Bioinformatics* 2021;**37**:1900–8.
91. Sharma K, Schmitt S, Bergner CG. *et al.* Cell type- and brain region-resolved mouse brain proteome. *Nat Neurosci* 2015;**18**:1819–31.
92. de Sousa Abreu R, Penalva LO, Marcotte EM. *et al.* Global signatures of protein and mRNA expression levels. *Mol BioSyst* 2009;**5**:1512–26.
93. Buccitelli C, Selbach M. mRNAs, proteins and the emerging principles of gene expression control. *Nat Rev Genet* 2020;**21**:630–44.
94. Liu Y, Beyer A, Aebersold R. On the dependency of cellular protein levels on mRNA abundance. *Cell* 2016;**165**:535–50.
95. Tabula Muris C, Overall C, Logistical C. *et al.* Single-cell transcriptomics of 20 mouse organs creates a Tabula Muris. *Nature* 2018;**562**:367–72.
96. Wu H, Tao J, Chen PJ. *et al.* Genome-wide analysis reveals methyl-CpG-binding protein 2-dependent regulation of microRNAs in a mouse model of Rett syndrome. *Proc Natl Acad Sci U S A* 2010;**107**:18161–6.
97. Rodrigues DC, Mufteev M, Weatheritt RJ. *et al.* Shifts in ribosome engagement impact key gene sets in neurodevelopment and ubiquitination in Rett syndrome. *Cell Rep* 2020;**30**:4179–4196.e11.
98. Wang H, Wang Y, Yang J. *et al.* Tissue- and stage-specific landscape of the mouse translatome. *Nucleic Acids Res* 2021;**49**:6165–80.
99. Harnett D, Ambrozkiewicz MC, Zinnall U. *et al.* A critical period of translational control during brain development at codon resolution. *Nat Struct Mol Biol* 2022;**29**:1277–90.
100. Wang ZY, Leushkin E, Liechti A. *et al.* Transcriptome and translatome co-evolution in mammals. *Nature* 2020;**588**:642–7.
101. Ho JJD, Balukoff NC, Theodoridis PR. *et al.* A network of RNA-binding proteins controls translation efficiency to activate anaerobic metabolism. *Nat Commun* 2020;**11**:2677.
102. Goodpaster BH, Sparks LM. Metabolic flexibility in health and disease. *Cell Metab* 2017;**25**:1027–36.
103. Smith RL, Soeters MR, Wust RCI. *et al.* Metabolic flexibility as an adaptation to energy resources and requirements in health and disease. *Endocr Rev* 2018;**39**:489–517.
104. Bulow P, Patgiri A, Faundez V. Mitochondrial protein synthesis and the bioenergetic cost of neurodevelopment. *iScience* 2022;**25**:104920.
105. Goyal MS, Hawrylycz M, Miller JA. *et al.* Aerobic glycolysis in the human brain is associated with development and neotenous gene expression. *Cell Metab* 2014;**19**:49–57.
106. Kuzawa CW, Chugani HT, Grossman LI. *et al.* Metabolic costs and evolutionary implications of human brain development. *Proc Natl Acad Sci U S A* 2014;**111**:13010–5.
107. Oyarzábal A, Musokhranova U, Lf B. *et al.* Energy metabolism in childhood neurodevelopmental disorders. *EBioMedicine* 2021;**69**:103474.
108. Olson KA, Schell JC, Rutter J. Pyruvate and metabolic flexibility: illuminating a path toward selective cancer therapies. *Trends Biochem Sci* 2016;**41**:219–30.
109. Jeon JH, Thoudam T, Choi EJ. *et al.* Loss of metabolic flexibility as a result of overexpression of pyruvate dehydrogenase kinases in muscle, liver and the immune system: therapeutic targets in metabolic diseases. *J Diabetes Investig* 2021;**12**:21–31.
110. Ashrafi G, de Juan-Sanz J, Farrell RJ. *et al.* Molecular tuning of the axonal mitochondrial Ca(2+) uniporter ensures metabolic flexibility of neurotransmission. *Neuron* 2020;**105**:678–687.e5.
111. Diaz-Garcia CM, Meyer DJ, Nathwani N. *et al.* The distinct roles of calcium in rapid control of neuronal glycolysis and the tricarboxylic acid cycle. *elife* 2021;**10**:e64821.
112. Chao HT, Zoghbi HY, Rosenmund C. MeCP2 controls excitatory synaptic strength by regulating glutamatergic synapse number. *Neuron* 2007;**56**:58–65.